FINAL TECHNICAL REPORT

TO

THE US DEPARTMENT OF THE NAVY
## OFFICE OF NAVAL RESEARCH

AUGMENTATION AND CONTROL OF BURN RATE IN PLASMA-DEVICES

"Contract N00014-95-1-1221"

Mohamed A. Bourham
and
John G. Gilligan
North Carolina State University
Department of Nuclear Engineering
Raleigh, NC 27695-7909

19990527 044
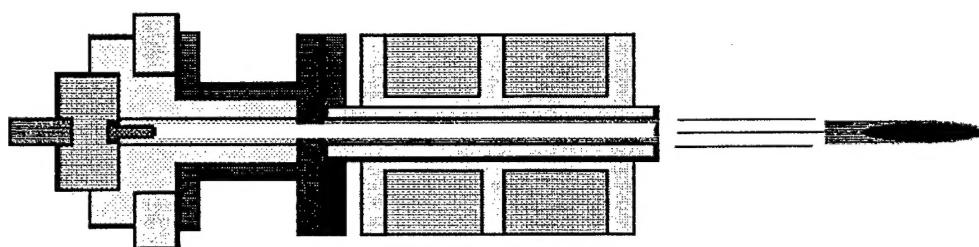
May 1999

REPORT DOCUMENTATION PAGE

Public reporting burden for this collection of information is estimated to average 1 hour per response, including the time for reviewing instructions, searching existing data sources, gathering and maintaining the data needed and completing and reviewing the collection of information. Send comments regarding this burden estimate or any other aspect of the collection of information, including suggestions for reducing the burden to Washington Headquarters Services, Directorate for Information Operations and Reports, 1215 Jefferson Davis Highway, Suite 1204, Arlington, VA 22202-4302 and to the Office of Management and Budget, Paperwork Reduction Project (0704-0188), Washington, DC 20503.

1. AGENCY USE ONLY (Leave blank)	2. REPORT DATE 10 May 1999	3. REPORT TYPE AND DATES COVERED Final Technical Report, 07/01/95- 12/31/99

4. TITLE AND SUBTITLE OF REPORT
Augmentation and Control of Burn Rates In Plasma Devices

5. FUNDING NUMBERS
N00014-95-1-1221

6. AUTHOR(S)
Mohamed A. Bourham

7. PERFORMING ORGANIZATION NAME(S) AND ADDRESS(ES)
North Carolina State University
Department of Nuclear Engineering
Raleigh, NC 27695-7909

8. PERFORMING ORGANIZATION REPORT NUMBER:

9. SPONSORING/MONITORING AGENCY NAME(S) AND ADDRESS(ES)
Office of Naval Research
Mechanics & Energy Conversion
800 North Quincy Street
Arlington, VA 22217-5660

10. SPONSORING/MONITORING AGENCY REPORT NUMBER:

11. SUPPLEMENTARY NOTES:
The views, opinions and/or findings contained in this report are those of the author(s) and should not be construed as an official Department of the Navy position, policy, or decision, unless so designated by other documentation.

12a. DISTRIBUTION AVAILABILITY STATEMENT
Approved for public release; distribution unlimited.

12b. DISTRIBUTION CODE

13. ABSTRACT (Maximum 200 words)

Interaction of electrothermal plasmas with solid propellants necessitates thorough understanding of plasma-propellant interface physics, momentum and energy transfer, plasma flow regimes, and mixing processes. High heat fluxes produced from electrothermal plasmas may enhance the propellant's burn rate via radiation, but limitation on enhencement might be limited by the effectiveness of the vapor shield mechanism.

This report provides experimental studies on plasma-propellant interaction utilizing the North Carolina State University (NCSU) Plasma-Propellant Interaction Experiment "PIPE", which is a plasma-chemical device that has been constructed to investigate the physics taking place at the plasma-propellant interface in plasma-chemical systems. The study provides an investigation of the effect of plasma on the burn rates of solid propellants as a function of plasma parameters, and decoupled effect of plasma pressure and temperature on observed burn rates of JA-2 solid granular propellant. Theory and code development include a psuedo 2-D, time dependent plasma source code that predicts plasma parameters, and a 2-D turbulent boundary layer code with coupled radiation transport.

14. SUBJECT TERMS
ETC Guns, Propellant Burn Rates, Radiative Heating, Plasma Flow.

15. NUMBER OF PAGES 48

16. PRICE CODE

17. SECURITY CLASSIFICATION OF REPORT: UNCLASSIFIED	18. SECURITY CLASSIFICATION OF THIS PAGE UNCLASSIFIED	19. SECURITY CLASSIFICATION OF ABSTRACT UNCLASSIFIED	20. LIMITATION OF ABSTRACT UL

STANDARD FORM 298 (REV 2-89)

FINAL TECHNICAL REPORT

TO

THE US DEPARTMENT OF THE NAVY
OFFICE OF NAVAL RESEARCH

AUGMENTATION AND CONTROL OF BURN RATE IN PLASMA-DEVICES

"Contract N00014-95-1-1221"

Mohamed A. Bourham
and
John G. Gilligan
North Carolina State University
Department of Nuclear Engineering
Raleigh, NC 27695-7909
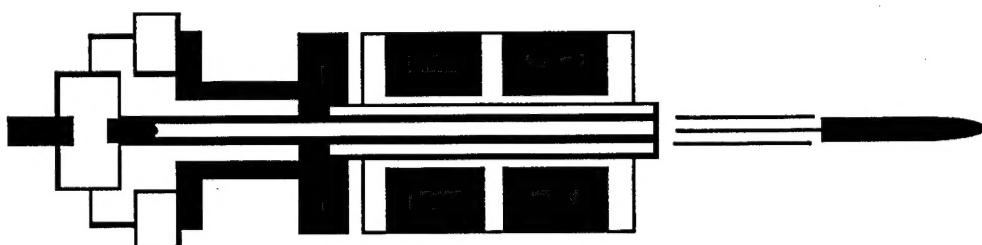
May 1999

ACKNOWLEDGMENT

TABLE OF CONTENTS

AUGMENTATION AND CONTROL OF BURN RATE IN PLASMA-DEVICES

Final Technical Report

by

Mohamed A. Bourham and John G. Gilligan

North Carolina State University, Department of Nuclear Engineering
Raleigh, N. C. 27695-7909

Prepared for

**North Carolina State University
Department of Nuclear Engineering
Raleigh, NC   27695-7909**

May 1999

ABSTRACT

Plasma-chemical devices are devices that exhibit generation of high density, high enthalpy flows. Such devices may provide possible useful propulsion applications in hypersonic launch technology, rocket propulsion, pulsed electrothermal launchers and electrothermal-chemical guns. Interaction of electrothermal plasmas with solid propellants necessitates thorough understanding of plasma-propellant interface physics, momentum and energy transfer, plasma flow regimes, and mixing processes. High heat fluxes produced from electrothermal plasmas may enhance the propellant's burn rate via radiation, but limitation on enhencement might be limited by the effectiveness of the vapor shield mechanism.

This report provides experimental studies on plasma-propellant interaction utilizing the North Carolina State University (NCSU) Plasma-Propellant Interaction Experiment "PIPE", which is a plasma-chemical device that has been constructed to investigate the physics taking place at the plasma-propellant interface in plasma-chemical systems. The study provides an investigation of the effect of plasma on the burn rates of solid propellants as a function of plasma parameters, and decoupled effect of plasma pressure and temperature on observed burn rates of JA-2 solid granular propellant. Theory and code development include a psuedo 2-D, time dependent plasma source code that predicts plasma parameters, and a 2-D turbulent boundary layer code with coupled radiation transport.

I. INTRODUCTION

Interaction between electrothermal plasma and energetic materials, described as a plasma-chemical discharge system, may provide possible ways for the generation of high density, high enthalpy flows. Extensive research on plasma-chemical interaction may lead to the viable operation of many propulsion devices and various propulsion applications, e.g. ETC guns, rocket propulsion, pulsed electrothermal thrusters, and hypersonic mass acceleration technology [1-7]. Energy transfer and mixing processes in plasma-chemical reactions are complex. Intensive research in plasma-propellant interaction can provide better understanding of the plasma-chemical reaction process, mass acceleration optimization to achieve higher velocities, a control of the burn rate of propellants), plasma-chemical boundary layer processes and role of the flame-vapor shield.

A plasma-propellant discharge system is a device where high-density, low-temperature plasma is injected into a selected combustible agent (propellant). The plasma generator for such systems is usually capillary discharge. Typical densities of 10^{25}-10^{26}/m^3 and temperatures of 1-3 eV: 11,600-34,800°K are achievable in capillary discharges, and the plasma flow can serve as an external high heat flux source [8-11]. Under high heat flux irradiation from plasmas, a vapor shield of evaporated material protects the material surface by reducing the energy transport through the boundary layer vapor shield [12-15]. In the case of chemical combustible materials, it is possible that such external high heat fluxes from the plasma can provide enhanced burn rate, howecer, the burn rate may be limited by the vapor shield at the combustion flame temperature, and will be refered to a "flame vapor shield effect".

A plasma-chemical device "**PIPE, Plasma-Propellant Interaction Experiment**" has been constructed, and tested for operation, to investigate the physics taking place at the plasma-propellant interface in plasma-chemical systems [8,16,17]. It uses a 340μF capacitor that can be charged up to 10 kV to provide 17 kJ of stored energy. The capacitor is discharged via a spark-gap switch and provides a current up to 100 kA over 100-120 μs pulse length. The plasma source consists of an insulating replaceable cylindrical sleeve which slides inside of a polycarbonate (Lexan) cylinder. The electrodes at each end of the sleeve are made of HD-17 tungsten alloy (90% tungsten, 6% nickel, and 4% copper), and the spacing between the electrodes is 12 cm long and has an inner diameter of 4 mm. The power densities, temperatures and pressures in the PIPE facility are sufficient to simulate typical conditions of plasma-chemical devices.

The ET plasma source injects the plasma into a cubic chamber which accommodates a propellant test stand. Access to various diagnostics includes fiber optics for optical emission spectroscopy, BNC's for strain gauges, and absolute pressure transdusers, instrumentation feedthroughs for fast and infrared thermocouples, and external standard discharge current and voltage diagnostics. The energy transmission factor through the vapor shield inside the ET source is about 10% at lower energy inputs and decreases to 5% at higher energies, which compares favorably with results obtained from similar sources on separate ET experiments, as well as the predictions of various capillary discharge codes [18-27].

II. THE EXPERIMENTAL FACILITY "PIPE"

The ET plasma source (capillary) contains a replaceable cylindrical insulator (Lexan sleeve), which slides inside of the Lexan main insulator. A fresh replaceable sleeve is used for each shot. The ET plasma is injected into the propellant surface at different angles of incidence. A 90° exposure (perpendicular) gives a maximum momentum transfer effect, while a 0° exposure (parallel) maximizes energy transfer to the surface. Fig. 1 shows a cutaway of the plasma-chemical interaction experiment "PIPE" [7,8]. A plasma-propellant test chamber is connected to the source.

3

The chamber contains a 3-D positioning pivot test stand with propellant samples on the top of the testbed. Positioning is necessary so that the heat flux can be varied easily from high (close to the plasma) to low (farther away). Standard measurements include discharge current and voltage, where current and voltage are measured via a Rogowski coil and a calibrated potential divider, respectively. Current, voltage, thermocouples, strain gauges, pressure transducers and photomultiplier signals are connected to LeCroy waveform digitizers. The pulse length can be varied using switchable capacitor modules and voltages can be varied from a few hundred volts to a few kilovolts. A modification to the experiment has been implemented adding a second expansion chamber to allow for further plasma expansion and increased diagnostics access, as shown in Fig. 1. A detailed drawing of the electrothermal plasma generator section is also shown.
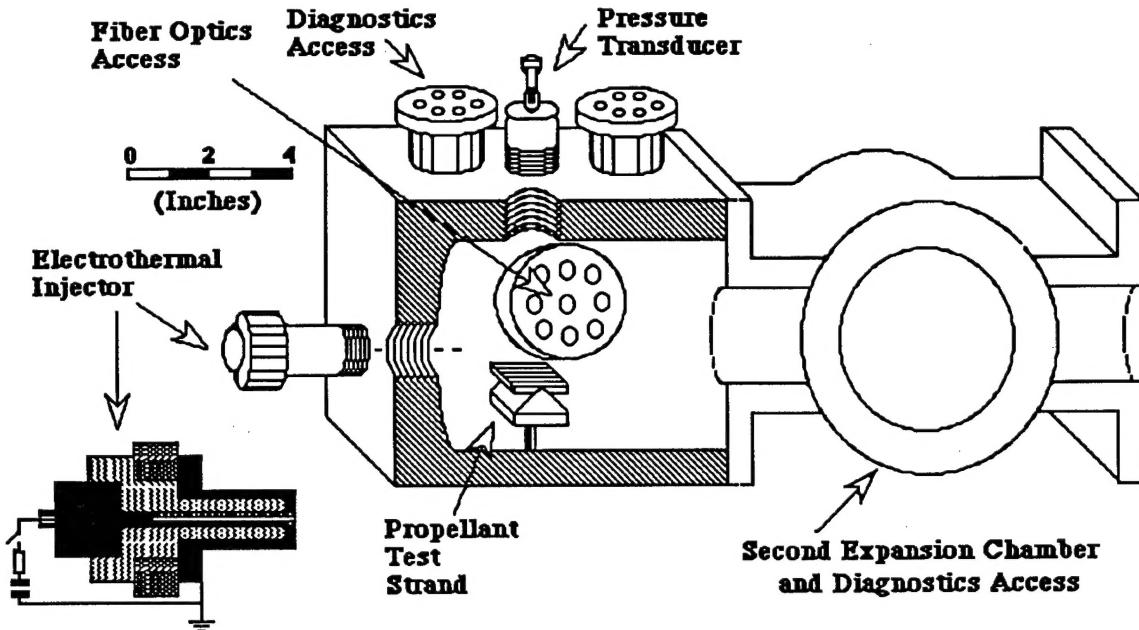
Fig. 1 Isometric cutaway view of the PIPE facility, showing the propellant test stand, an absolute pressure transducer for chamber pressure, second expansion chamber, diagnostics access, and detailes of the plasma generator section.

III. BURNRATE EXPERIMENTS ON JA-2 SOLID GRANULAR PROPELLANT

The direct method, at fixed pressure, can be used to measure the burn rate of the propellant. Burning is monitored visually or via burnthrough wires or mass loss [10-11,17-18, 28-31]. These methods may be more accurate than direct methods provided that the pressure is maintained constant. In the case of plasma injection into the propellant under vacuum, the burn process continues only during the discharge time over the current pulse time [11,17]. This is because the pressure at the propellant's surface is high enough for increased burn rate, and the burn extinguishes after the discharge as the pressure drops back to vacuum conditions. In such a case, the burn will be incomplete and the mass loss of the propellant can be measured. Fig. 2 shows the burn rate of JA-2 solid propellant with plasma injection compared to the burn rate for conventional ignition [16,17]. The burn rate has been calculated from the evolved mass, where the mass loss is transferred to ablation thickness, over a discharge period of 400 μs, assuming that the burn process takes place during that time, which represents an average estimate of the burn rate. However, plasma augmentation to solid propellants burn rate is evident from such measurements that show an increase in the burn rate by a factor of three at a surface pressure of 10,000 psi.

4
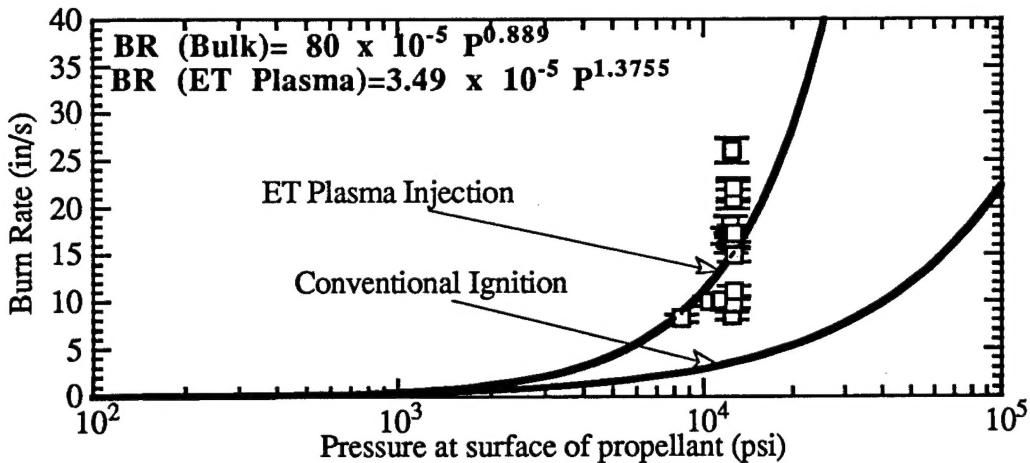
Fig. 2 Measured burn rate of a solid propellant ignited with ET plasma injection as a function of the pressure at the propellant's surface, compared to the burn rate of the same propellant with conventional ignition.

The evaluation of burn rate, based on the measured evolved mass, is valid when comparing the total mass loss to the mass loss due to ablation. For a known incident heat flux, the amount of erosion from the surface of the propellant due to sublimation of the propellant is only about 10% of the total mass loss. The calculated erosion thickness due to burn releases an amount of energy that compares favorably with the energy due to pressure increase inside the combustion chamber. This suggests that the measured burn rate is valid, as an average burn rate over 400 μs, which is the time average of the applied pressure at the surface of the propellant. This measured burn rate implies that radiative heating of the propellant's bed is the main reason for observed enhanced burn rates.

A set of experiments were conducted on the propellant where the plasma was injected onto the propellant bed at various angles. This analysis compares the experimentally measured plasma temperature, density and pressure to the code predicted values. The 1-D, time dependent code SODIN [18,19] has been used to predict the plasma parameters of the source for the shots when the plasma is injected into the propellant surface at different inclination angles. The experimental values of the plasma parameters, temperature and density, were obtained from optical emission spectroscopy measurements [32-35]. Because of the fact that the plasma is optically thick, the optical emission spectroscopy data are indicative of the plasma boundary layer, and hence, obtained parameters are those for the boundary layer [36-40]. Time-averaged boundary layer temperatures of 8,800 to 14,000 °K ($\approx$ 0.8 - 1.2 eV) and plasma densities of 2 x 10^{23} to 4.5 x 10^{23} m^{-3} have been deduced by measurements along the axis of the device using the relative intensities and the Stark broadening of the copper lines. Fig. 3 shows the plasma temperature calculated using a Boltzmann plot of neutral copper lines and a match of CO_2 emission predictions with the data, while Fig. 4 shows the plasma density calculated from the Stark broadening of neutral copper lines and matching CO_2 emission predictions with data [33-35].
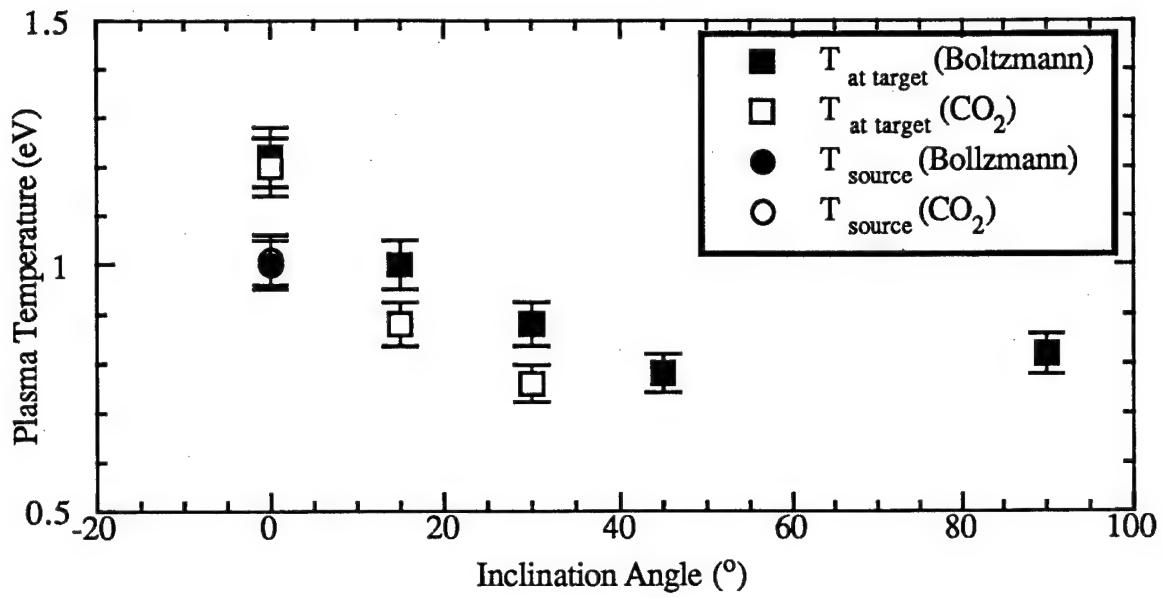
Fig. 3 Plasma temperature calculated using a Boltzmann plot of neutral copper lines and a match of CO_2 emission predictions with the data.
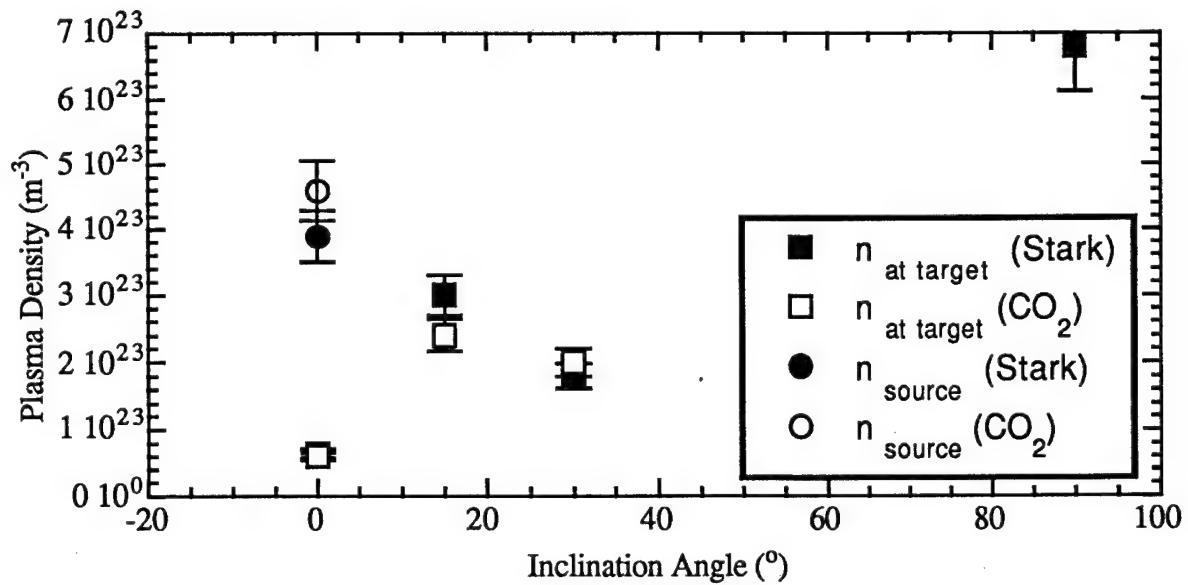
Fig.4 Plasma density calculated from the Stark broadening of neutral copper lines and matching CO_2 emission predictions with data.

Comparisons with the measured burn rates of the JA-2 propellant versus the inclination angle suggests a stronger correlation of plasma burn rate with plasma kinetic pressure than with the radiative heat flux. Estimates of the temperatures and densities for some shots were analyzed by observing the C_2 Swan Bands. The data were compared with synthetic spectra calculated using the UVCODE molecular spectra-radiative transport code [41]. The plasma temperature calculated using a Boltzmann plot of neutral copper lines correlates well to that obtained from CO_2 emission predictions with the data. The plasma density calculated from the Stark broadening of neutral copper lines correlates also well to that obtained from CO_2 emission predictions with data. Both plasma temperature and density decrease with increased angles of injection. The plasma pressure and the source heat flux are calculated by SODIN code for the same shots. SODIN code calculates the plasma parameters using the discharge current data file as an input to the code, and solves the set of governing equations self consistently. The average pressure for these shots is about 125 ± 25 MPa, peak plasma pressure is 250 ± 50 MPa, and source heat flux is 28 ± 6 GW/m^2. Fig. 5 shows the plasma pressure (peak and average) and source heat flux as predicted by SODIN Code for shots taken at different angle of inclination. The values calculated by the code are those at the source exit (last node in the source), and are typical and consistent for shots at 5 kJ input energy to the source.
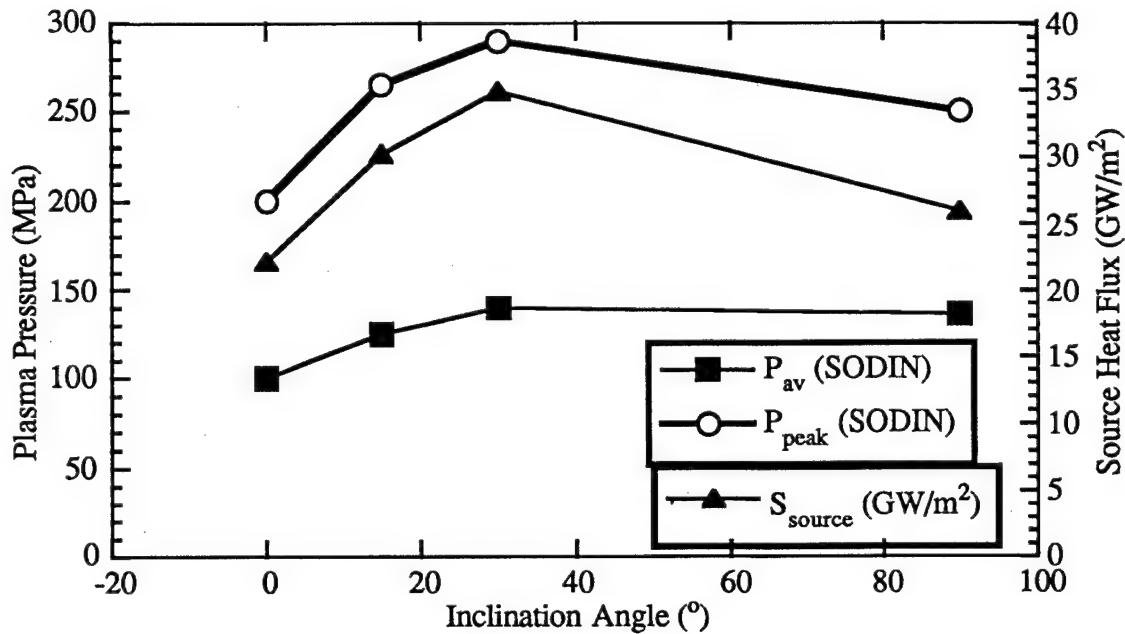
Fig. 5 Plasma pressure (peak and average) and source heat flux as predicted by SODIN Code for shots taken at different angle of inclination.

The core plasma temperature, as predicted by SODIN Code, is compared to the plasma boundary layer temperature calculated from optical emission spectroscopy. Fig. 6 displays the plasma temperature (core plasma) as predicted by SODIN Code compared to that calculated from Optical Emission Spectroscopy (plasma boundary). The average core plasma temperature is about 1.7 ± 0.1 eV, while the plasma boundary layer temperature varies from 1.24 eV at 0° to 0.8 eV at 90°. In fact, the average plasma boundary layer temperature has an average of 0.88 ± 0.1 eV over the entire range of injection angle except at 0° where it has a higher value (1.24 eV). The difference between temperatures (core and boundary) suggests that the boundary layer plays a role in absorbing a substantial fraction of the incoming heat flux (vapor shield mechanism), which is typical for ablating surfaces under high heat flux irradiation. This vapor shield mechanism would then reduce the effectiveness of radiative heating on the propellant.
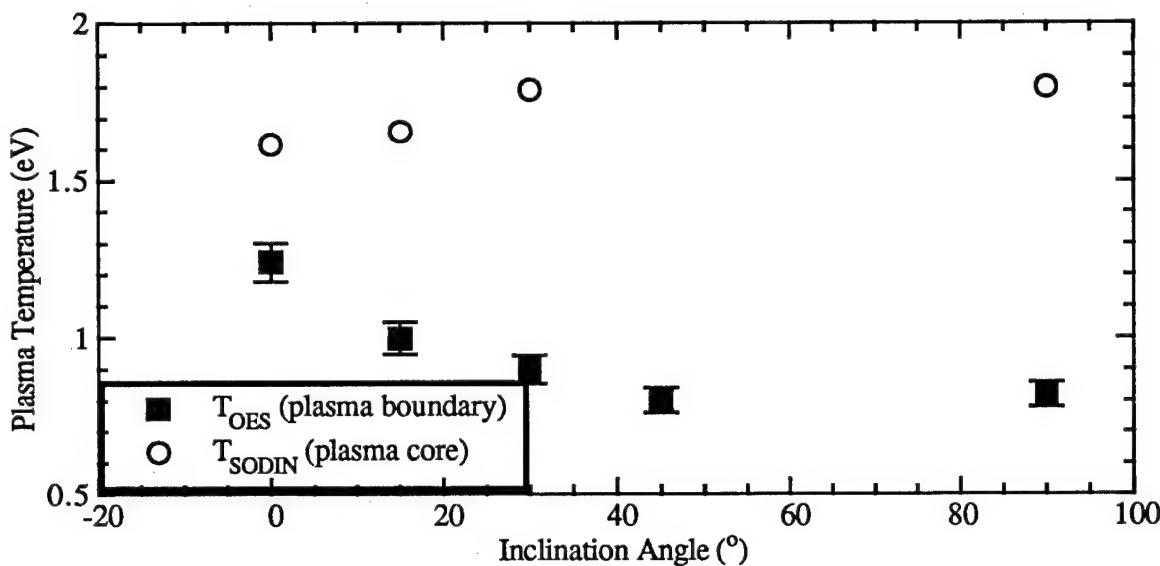
Fig. 6 Plasma temperature (core plasma) as predicted by SODIN Code compared to that calculated from Optical Emission Spectroscopy (plasma boundary).

In order to estimate the effectiveness of the vapor shield, the core and boundary layer plasmas are both assumed to radiate as a blackbody such that the heat flux of the source and the boundary are scaled to the temperature by Stephen-Boltzmann's law. The source fluence may be expressed as: $q''_{(source)} = \sigma (T_{SODIN})^4$, where T_{SODIN} is the core plasma temperature at the source exit, and σ is the Stephen-Boltzmann's constant. The heat flux at the boundary layer is given by: $q''_{(boundary)} = f \sigma (T_{boundary})^4$, where $T_{boundary}$ is the boundary layer temperature as calculated from spectroscopy measurements, and f is the energy transmission factor through the vapor shield layer. An estimate of the energy transmission factor can be obtained from the ratio between the boundary layer heat flux to the source flounce: $f = q''_{(boundary)} / q''_{(source)}$. Fig. 7 shows a plot of the energy transmission factor f through the developed vapor layer (plasma boundary layer) calculated from the ration between the surface heat flux (at the boundary) and the core plasma heat fluence.

It is clear that the energy transmission factor is about 10% and less for angles between 15 and 90°, which is also expected for most ablating surfaces when a vapor shield layer is developed and reaches steady-state. The highest value obtained for the factor f is 35% at 0°, which correlates to results observed for most graphite surfaces at such inclination angle. The obtained values of the factor f suggest that radiative heating may be limited during the burn of the propellant due to limited energy transport to the surface, and that plasma kinetic pressure has a stronger effect on the burn rate than the plasma radiative heat flux.
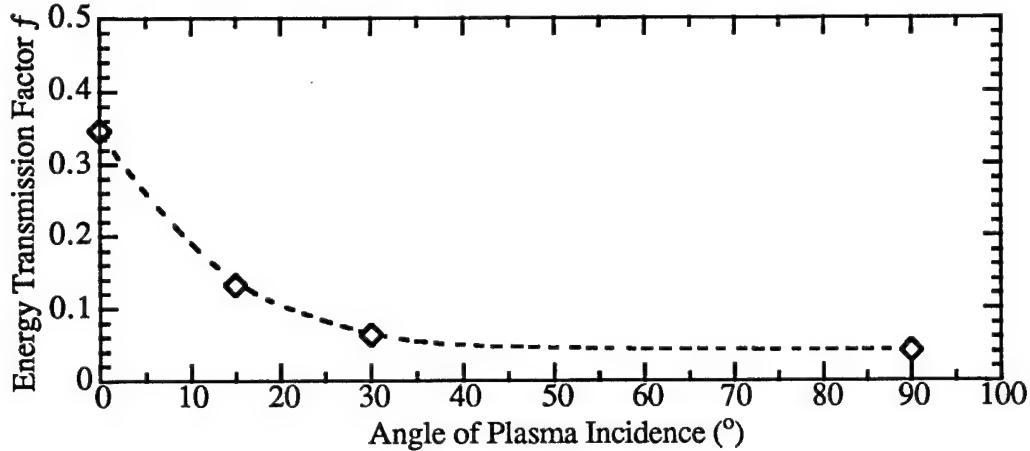
Fig. 7 Energy transmission factor f through the developed vapor layer (plasma boundary layer) calculated from the ration between the surface heat flux (at the boundary) and the core plasma heat fluence.

IV. RADIATIVE HEATING AND DECOUPLING EXPERIMENTS

In the previous section, an analysis of the vapor shield effect has shown that the energy transmission factor through the vapor shield is about 10% at normal incidence pf the plasma to the propellants sfurface. This may suggest that radiative heating may be limited during the burn of the propellant due to limited energy transport to the surface. Experiments have shown increased burn rate with increased plasma pressure when injection is normal to the surface of the propellant, as shown in Fig. 2. In order to compare burn rates at various pressures, a plot of the burn rate as a function of plasma pressure at the surface is shown in Fig. 8 below. Due to the fact that the vapor shield may reduce the effectiveness of radiative transport to the surface, as has been shown by the energy transmission factor, it might be concluded that the increase in burn rates is dominated by the plasma kinetic pressure. However, it is apparent that radiative heating plays a major role in enhanced burn rates [5,11,28,31,42]. In order to investigate the temperature effect, one has to investigate the burn rate as a function of plasma temperature for the same set of data shown in Fig. 8. Plasma temperatures for same data set were obtained from the code, which predicts the core plasma temperature, as displayed in Fig. 9 below. It is clear from Fig. 9 that the burn rate increases with increased plasma temperature, and matches the same increasing trend observed with increased pressure. This suggests that radiative heating is responsible for enhanced burn rates. However, the plasma density for these shots is also increasing with increased pressure, and a coupled pressure-temperature effect is still dominant.
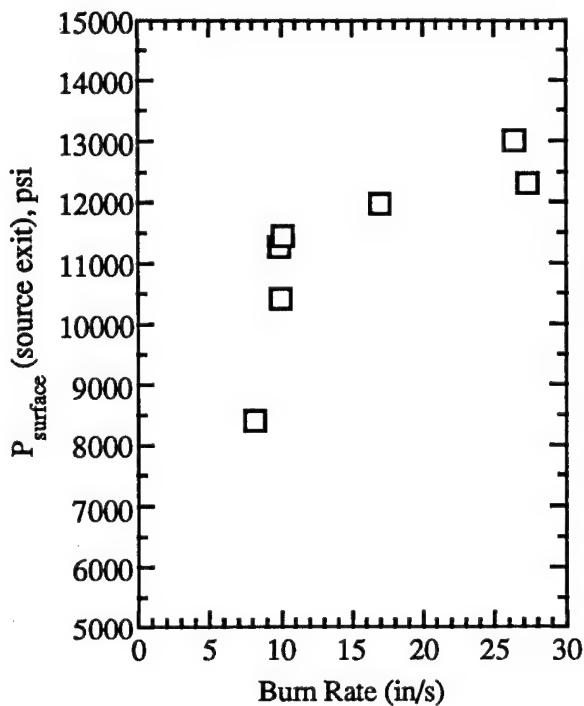
Fig. 8 Burn rate of JA-2 solid propellant as a
function of plasma pressure at the surface
of the propellant.
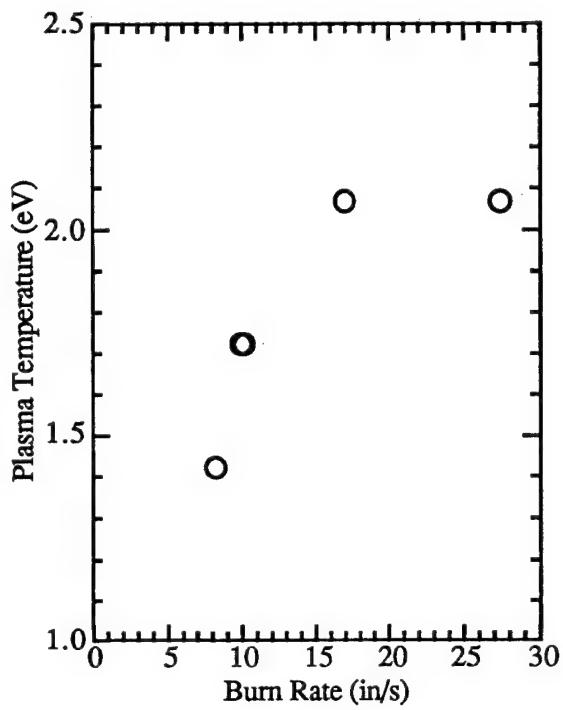
Fig. 9 Burn rate of JA-2 solid propellant
as a function of plasma temperature

In order to asses radiative heating versus pressure effect on burn rates, a set of decoupling experiments were designed to decouple pressure-temperature using moderating attachements [42]. Barrel section attachments can be used to change either the pressure or the temperature for a given input energy to the plasma source. A straight moderator barrel attached to the source allows for extended plasma flow, at the same pressure, but reducing the plasma temperature via moderating material on the moderator barrel wall. An illustartion of the staright moderator is shown in Fig. 10. In order to maintain the plasma temperature and varying the pressure, a conical nozzle geometry may be used for a choked flow at the source exit, as shown in Fig. 11. In both straright and chocked attachements, an absolute pressure transducer is placed at the attachement's exit to measure the pressure.

ET Plasma   Moderator   Pressure
Source   Section   Attachment
                           with Pressure Transducer
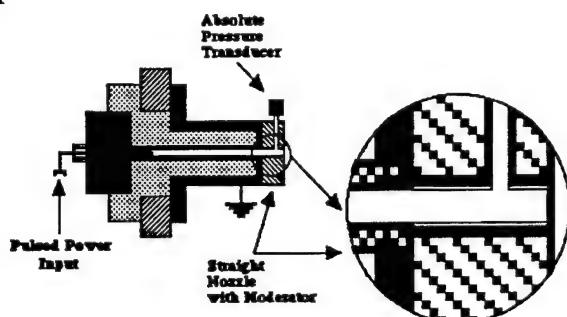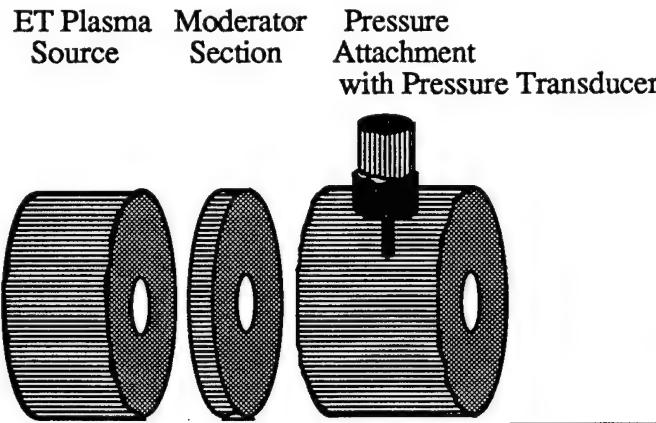
Fig. 10 Illustrative drawing showing staright barrel moderator attachment. Pressure transducer is situated close to the attachement exit.

10

Pressure Transducer

ET Plasma   Pressure Nozzle
Source   Attachment
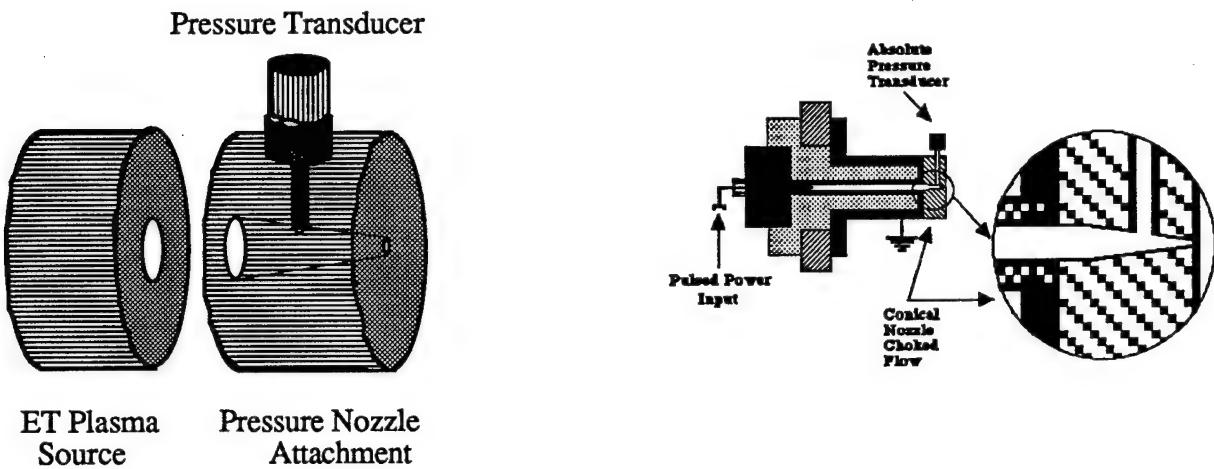
Fig. 11 Illustrative drawing showing choked flow conical nozzle attachment. Pressure transducer is situated close to the nozzle exit.

To show the difference in pressure between the two attachements, staright and nozzled, two shots were conducted at same input energy to the source, with a discharge current of 12-13 kA. The measured pressure peaks to 1000 psi for the straight attachment , and peaks to 2200 psi for the nozzle attachment. Fig. 12 shows the time history of the measured pressure for the choked flow nozzle, where the pressure peaks to 2200 psi in 0.4 ms.
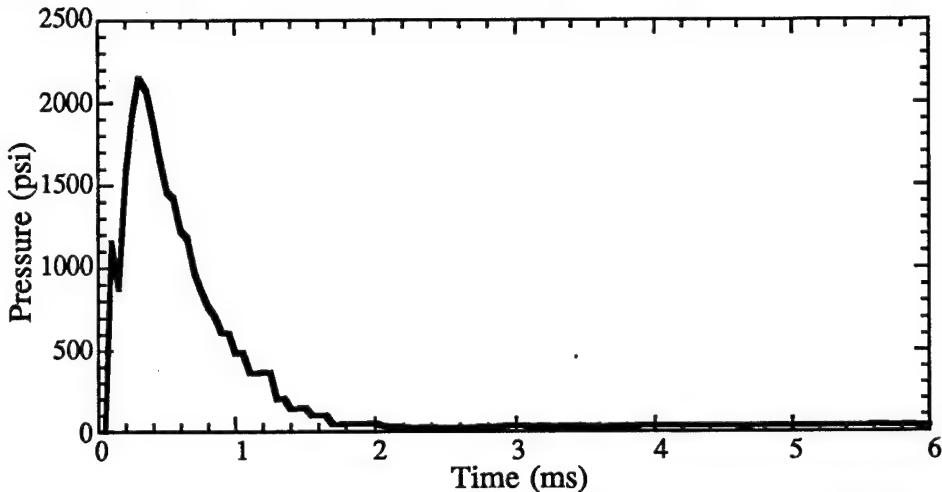
Fig.12 Measured pressure for choked flow nozzle, for an input energy of 3 kJ to the plasma source. Pressure peaks to 2200 psi in 0.4 ms.

Various straight barrel moderator materials were prepared with different barrel lengths, materials used are acrylic, Lexan "polycarbonate, polyethylene and ceramics "aluminum oxide". Shots taken with acrylic moderators proved to be inadequate for temperature moderation as acrylic can combust. Shots taken with Lexan polycarbonate moderators, and other polymers or ceramics, are more adequate. Standard electrical measurements are used to measure discharge current (Pearson probes and Rogowskii coils) and voltage (capacitively-coupled voltage probes). Fig. 13 shows the measured discharge current and voltage for a 3 kJ shot, and calculated power and integrated energy. In order to evaluate the source performance, system impedance and source resistance are calculated, as seen in Fig. 14 for discharge current and corresponding impedance, indicating about 120 mΩ resistance of the capillary of 4 mm bore and 9 cm length, which compares

11

well with typical capillary discharges. Optical emission spectroscopy is also taken during the moderators shots to measure plasma temperature and density and to compare to code predictions.
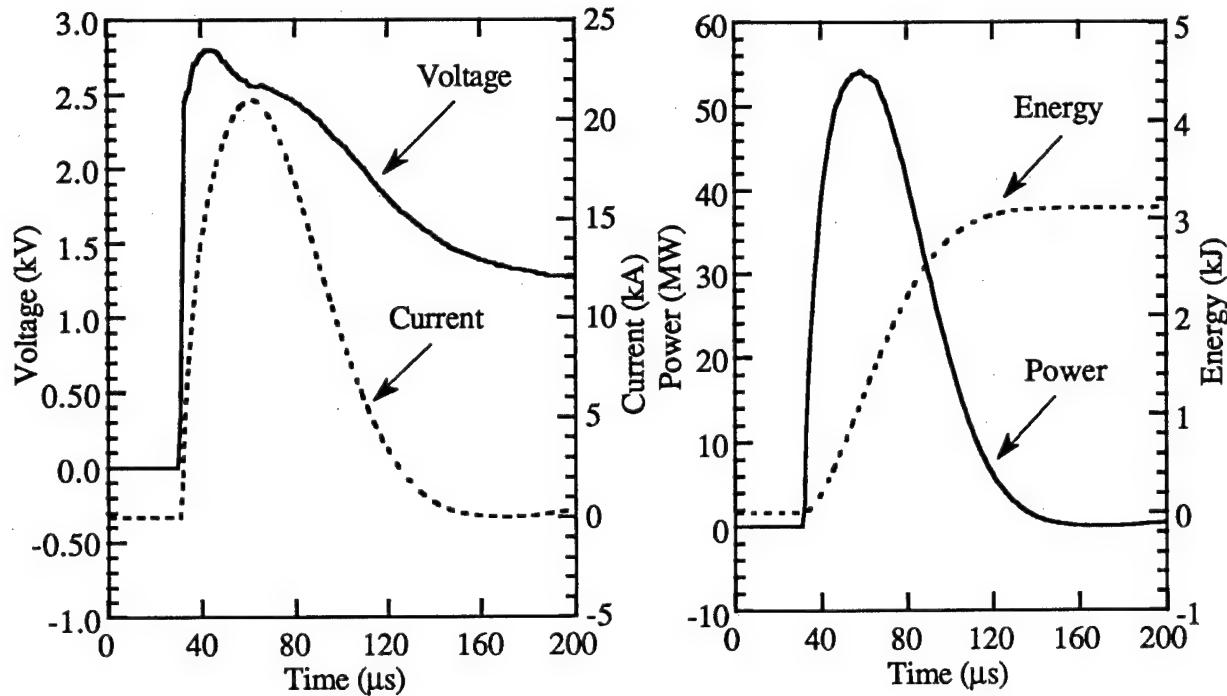
Fig. 13 Typical discharge current and voltage (left graph) for a 3 kJ shot (SHOT P162), and power and integrated energy (left graph) for same shot.
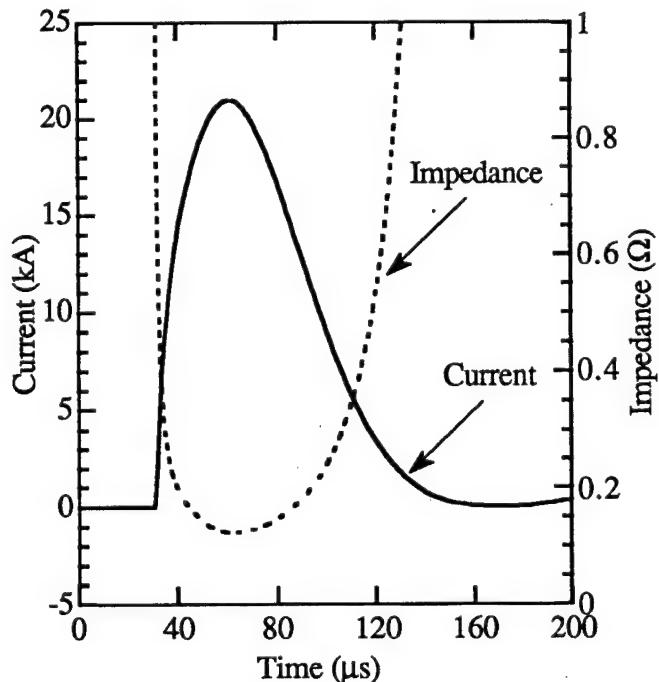
Fig. 14 Typical discharge current and corresponding impedance for 3 kJ shot (SHOT P162),

12

showing that the capillary resistance is about 120 mΩ at peak current.

The set of experiments on straight moderator barrels have been conducted using different moderator length of 1.91, 3.16 and 4.47 cm. Propellant sample is kept close to the source exit at a distance of 1.96 cm, where the plasma impacts normal to the propellant surface and some shots were conducted with propellant sample at a shorter distance from the source (0.27 and 0.77 cm). Input energy to the source is also kept constant at 6 kJ. The following table, Table 1, summarizes results of six shots , three were done by exposing one side of the propellant to the plasma, and three with the propellant exposed twice but to each side once. This table is a sample of the moderators results.

| Shot #	Pmax (MPa)	Pav (MPa)	Tmax (K)	Tav (K)	Moderator Length (cm)	Δm (mg)
JA-2 shot on one side:						
206	42	13.70	19000	9780	4.47	15.33
208	40	12.96	18000	10000	3.16	19.26
210	40	12.57	19000	10050	1.91	20.91
JA-2 shot one side then re-shot other side:						
207	38	12.81	18000	9454	4.47	22.42
209	43	13.44	19000	9932	3.16	24.96
211	39	12.44	19000	10132	1.91	24.27

It is obvious that moderator sections have been successful in maintaining an average constant pressure while the average plasma temperature varies. From shots 206, 208 and 210, erosive burn is increasing with increased plasma temperature at constant plasma pressure. Similar results for shots 207, 209 and 211 but with higher erosive burn. It is clear that radiative heating plays a major role in plasma-propellant interaction. When sample was exposed twice, at both ends, erosive burn is much higher than when exposed once indicating changes in sample kinetics. Evaluation of each shot is also conducted via our modified ODIN code (MODIN, 1-D, time dependent), where plasma parameters in the source and the moderator are evaluated.

V. ANALYSIS OF RADIATIVE HEATING AND DECOUPLING EXPERIMENTS

Experiments have been conducted using the electrothermal-chemical experimental facility, PIPE, to study the direct interaction between the electrothermal plasma and single grain monolithic JA-2 propellant to characterize the burn rate under plasma conditions. Such characterization is essential to clear the ambiguity about the mechanisms (mechanical-thermal or chemical) responsible for the burn rate enhancement. Decoupling of the pressure-temperature-effect has been investigated by attaching moderating sections with different lengths to the source exit to perturb plasma temperature and pressure prior to injection to the propellant surface. In-depth interaction between plasma radiation and propellant has been studied by re-exposing the propellant samples after being flipped so that the unexposed surface facing the injected plasma. Optical emission spectroscopy has been used to diagnose plasma parameters, and a modified 1-D time dependent ET code, that uses the current file as input, has been used to predict the plasma parameters before injection to the surface of the propellant. Results showed an increased gasification rate with increased plasma temperature even for lower pressures, as well as further increase in burn rate for the double-sided

13

exposed samples than the single-side exposed samples, a finding that promptly arises a question about the effect of in-depth plasma radiation-propellant interaction on burn rates. Scanning electron microscopy (SEM) micrographs of JA-2 exposed samples show erosion and in-depth changes of the propellant grain.

A fundamental step in the way of studying and understanding plasma-propellant interaction is to investigate the effects of plasma parameters on burn rates of solid propellants. Burning rates of gun propellants is commonly expressed in the form of de Saint Robert's equation, which simply is a relation between the burn rate and the pressure as: $r=bP^n$, and generally increases with initial propellant temperature in what is known as the effect of conditioning temperature or "temperature sensitivity" [29]. The aforementioned enhancement of burning rates of solid propellants by using ET plasma as igniter has been attributed, by many investigators, to the role of plasma radiation-propellant-interaction [5,11,28,31]. To explain the interaction between plasma radiation and the solid propellant and the origin of the enhancement of burn rate, G. P. Wren et al. [31] proposed two possibilities for such interaction that lead to the enhancement of burn. These two possibilities depend on the temperature conditioning effect and/or affecting the kinetics near the propellant surface. K. White et al. [10] showed that plasma radiation induces reactions in depth in JA-2 propellant, which causes both in-depth chemical and physical change in the propellant. These reactions occur in the time frame of hundreds of microseconds and have not shown a dramatic effect on burn rates as had been deduced from post irradiation closed chamber studies. Accordingly, the individual effects of plasma pressure and temperature on burning rates, as well as the possibility of plasma radiation-propellant-in-depth-interaction, have been given special attention in this study "under the contract with ONR". Plasma pressure and plasma temperature are two interrelated parameters. Hence, decoupling of pressure-temperature-effect becomes essential to understand the mechanisms responsible for burn rate enhancement. In the present study, decoupling of plasma pressure-temperature-effect, as well as in-depth interaction between plasma radiation and propellant and it's effect on the gasification rate of JA-2, has been investigated. Detailed experimental arrangement for decoupling experiments using moderator barrels are shown in Fig. 15, based on the principles explained in the preceding section.
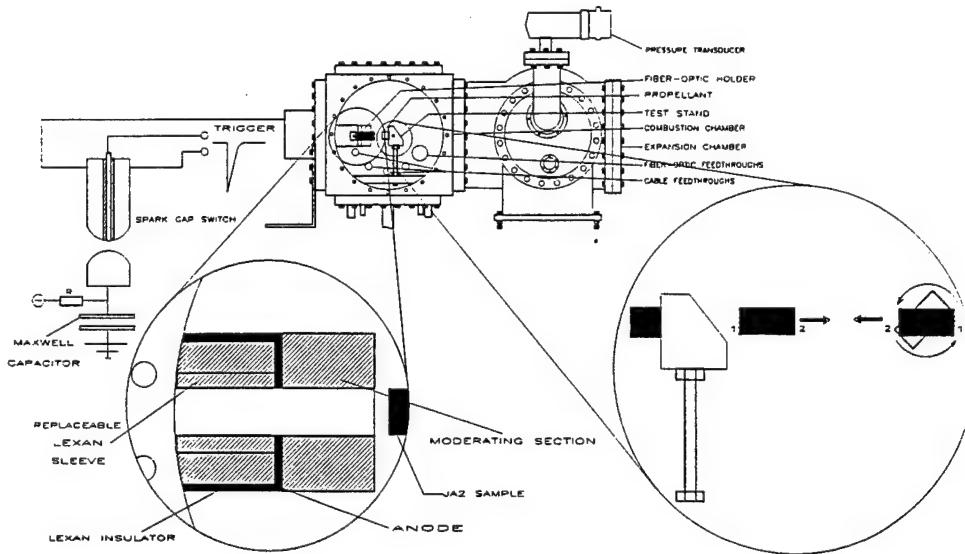

Fig. 15 Schematic diagram of the PIPE facility showing the main chamber, auxiliary chamber, moderator barrel section, and propellant stand. Left zoom shows the source section and moderating section. Right zoom shows the process of re-exposing samples.

14

The ET plasma is injected from the source section into an expansion chamber, where the propellant sample is situated close to the source exit. Decoupling of pressure-temperature-effect has been investigated by attaching moderating sections of Lexan polycarbonate [($C_{16}H_{14}O_3$)n] with different lengths to the source exit, as shown in the left zoom subplot of Fig. 15. The attached moderating section perturbs plasma temperature and pressure prior to injection into the propellant surface. Radiation loss from the plasma and the addition of cold ablated species from the moderator wall to the system act concurrently and lead to a decrease in plasma temperature. However, the addition of new particles increases the particle number density of the system. The effect of the increase of particle number density on the plasma pressure acts counter-currently to the effect of decreasing temperature with the result that the effect of increasing particle number density may do one of the following: 1) overcome the effect of decreasing temperature on the pressure and lead to the increase of pressure, or 2) compensate the effect of decreasing temperature on the pressure and the pressure remains constant, or 3) alleviate the effect of temperature decrease on the pressure. All of the above possibilities result in unbalanced effect on the plasma pressure and temperature. The technique used in studying plasma radiation-propellant interaction involves re-exposing the JA-2 propellant samples after being flipped so that the plasma is injected into the unexposed surface, as shown in the right zoom subplot of Fig. 15. Comparison between the gasification rate of the re-exposed sample and the single-side exposed sample, under same discharge conditions, rejects the effects of temperature sensitivity and surface kinetics since they are identical unless plasma radiation-propellant-in-depth-interaction occurs. Hence, differences in gasification rate between both cases can be attributed to in-depth interactions.

A series of experiments have been conducted involving single side and double side exposure of JA-2 samples to the ET plasmas, at the same discharge energy. For each moderator length the sample is exposed twice, one exposure for each side. A Tractor Northern TN-6500 Optical Multichannel analyzer (OMA) was used to observe the light emission from the plasma jetting out of the source when firing without moderator, or at the exit of the moderator section, when used. Light sampled from the bulk plasma intercepted by the optical fiber's solid angle view (20°) and the expanding ET plasma. This light is channeled through a single fiber-optic cable through a spectrometer onto a photodiode array. The array has 512 pixels which, (with a 600 grooves/mm reflection type grating) records the input energy (in the form of photons) over a 75nm range. This provides for a time integrated "snap shot" of the plasma emission during the shot [34,35]. The fiber optic cable was placed at the exit of the moderator section 90° relative to source axis, as shown in Fig. 15. Boltzmann plot technique was used to calculate the plasma temperature. Experiments were conducted at various input energies and the corresponding obtained plasma temperatures are shown in Fig. 16. Spectroscopy techniques used in ET plasma diagnostics are fairly reliable, and can provide important information about plasma composition, optical properties, as well as density and temperature. However, in such experiment, that has been designed to perturb plasma parameters, the experimental uncertainty associated with spectroscopic measurements makes it difficult to depend on these measurements in investigating the effect of plasma parameters on JA-2 burn rate. The modified 1-D, time-dependent code, MODIN, which is a modified version of ODIN code, has been used to predict the plasma parameters at the moderator exit [18,19]. The code uses the measured discharge current file as an input. The code predictions had been previously benchmarked with experimental measurements [18,19]. Fig. 17 shows plasma temperature as measured using spectroscopic techniques versus code predictions, where reasonable agreement, both in order of magnitude and trend, was obtained.
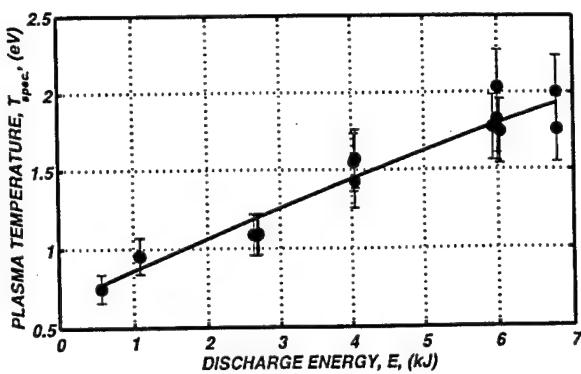
Fig. 16 Plasma temperature at source exit, obtained from spectroscopy, versus discharge energy.
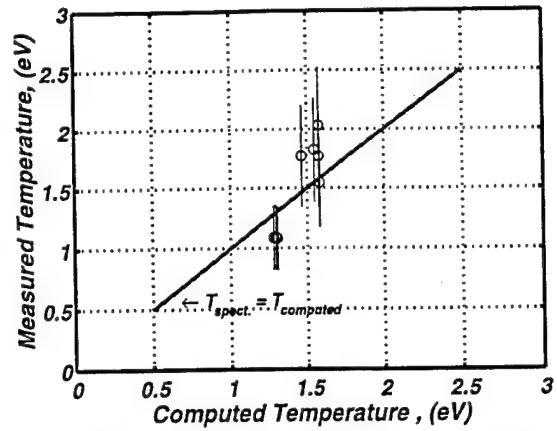
Fig. 17 Measured temperature from spectroscopy, versus computed temperature.

Spectra obtained at the source exit for low energy shots (0.565kJ) have shown C_2 swan band as emission lines, as indicated on Fig. 18. These bands are not very distinct, they tend to look like a bunch of closely packed lines, (limited by the system resolution). In practice they are very fine lines emitted by the rotational energy transitions of the molecular C_2. Those lines that are seen as emission lines in Fig. 18, are noticed to undergo self-absorption in a different experimental configuration (when moderating sections are attached to the source section), and at high energy shots (6.0kJ) as shown in Fig. 19.
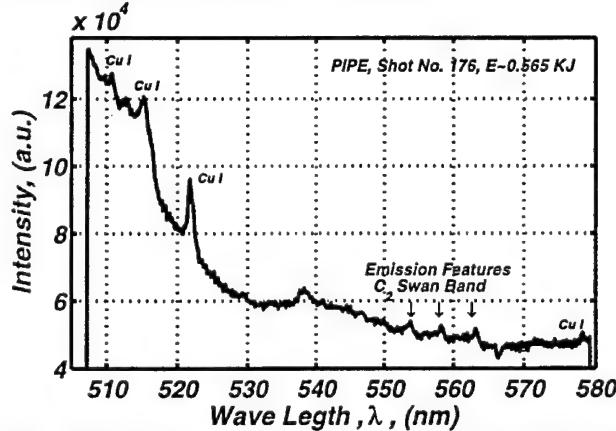
Fig. 18 Optical emission spectra obtained during a low energy (0.565kJ, 90° to axis)
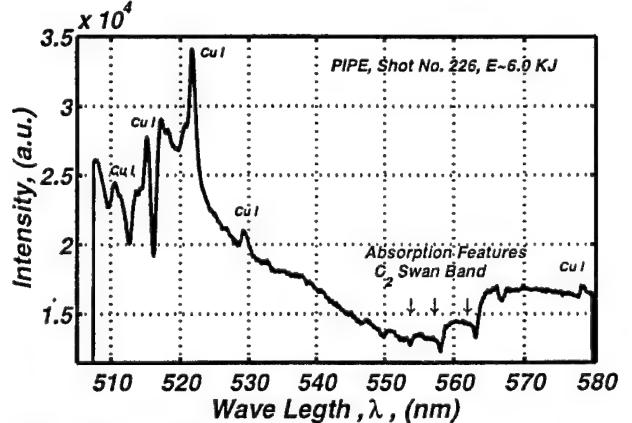
Fig. 19 Optical emission spectra obtained during a high energy shot with moderator section (6kJ, 90° to axis)

Cooling of the plasma in the moderating section and the increase of carbon atom concentration, due to ablation, in the boundary layer accelerate the recombination process and the production of C_2 molecules near the wall. The C_2 molecular species formed in the boundary layer absorb light (corresponding wavelength) emitted from the hot core. In Fig. 18, emission of these lines can be attributed to the radiative recombination of carbon species into C_2, while in Fig. 19, absorption of the lines is due to the formed C_2 species in the boundary layer of the plasma.

MODIN code has been used to compute the plasma pressure and temperature at the source exit and exit of the moderating section prior to the injection into the surface of JA-2 samples. Fig. 20

16

shows the effect of increased moderator length on the computed average pressure and temperature, where it is clear that the average pressure was kept constant and the burn rate decreases with increased length of the moderator. The graphs in Fig. 20 also show the measured burn rate for single-side and double-side shots, where same results show that the burn rate follows the plasma temperature. This indicates that the burn rate is more affected by the plasma radiative heating. These graphs may also be re-drawn in terms of an equivalent black-body radiation (T^4) to indicate the burn rate as related to radiation flux.

Single-side shots   Double-sided shots
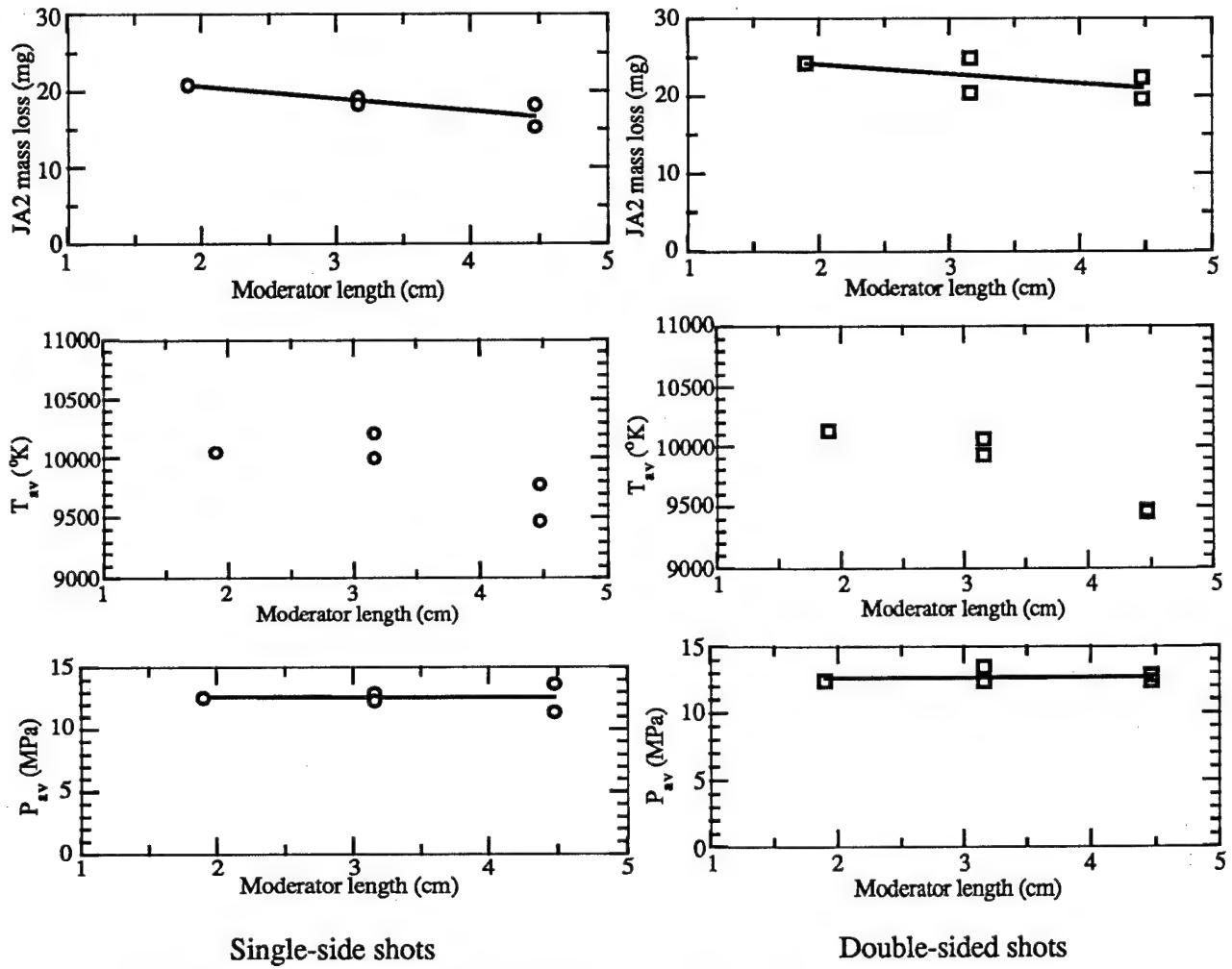
Fig. 20 Measured burn rate versus moderator's length and variation of plasma temperature and pressure. Results for samples shot single-side are shown on the left graphs, and samples shot double-sided are shown on the right graphs.

The value of $(T^4)_{av}$ can been chosen to represent the radiation term, where $(T^4)_{av}$ is the equivalent average radiation flux of a black-body. Linear fitting has been used in the figure to illustrate the general trend of the data points in each of the above subplots. It is evident that $(T^4)_{av}$, which follows Temperature (T) on the graph, decreases considerably with the increase of moderator length, as expected. However, the plasma average pressure remains approximately constant. By establishing such perturbation in average pressure and temperature values "P_{av} and $(T^4)_{av}$" before injection to the propellant surface, decoupling of the pressure-temperature-effect,

17

and the study of the individual effects of these two parameters, namely pressure and temperature, on the gasification rate of JA-2 single grains becomes applicable.

For PIPE experiments with the propellant grain situated in the expansion chamber, the burn of JA-2 does not complete and it ceases by the end of the discharge pulse. Under these conditions, the propellant mass loss gives expression to the average gasification rate in different shots using the same pulse length. As shown in Fig. 20, two data sets are presented, one for single-side exposed samples while the other is for double-sided exposed samples. Two distinct features can be recognized:

1- within each set of data, the gasification rate of JA-2 decreases with increased moderator length or, in other words, the gasification rate of JA-2 decreases with decreased plasma average radiant temperature.

2- the gasification rate of the double-sided exposed samples always shows greater values than it does with the single-side exposed samples, which suggests an effect of plasma radiation-propellant-in-depth-interaction on burn rate.

For now, the quick conclusion is that plasma radiation affect the propellant gasification rate and plays a role in burn rate enhancement. However, this quick conclusion is driven from the general trend of data points. More information can be obtained from the behavior of individual data points, as can be seen in Fig. 21 (a,b and c,d).
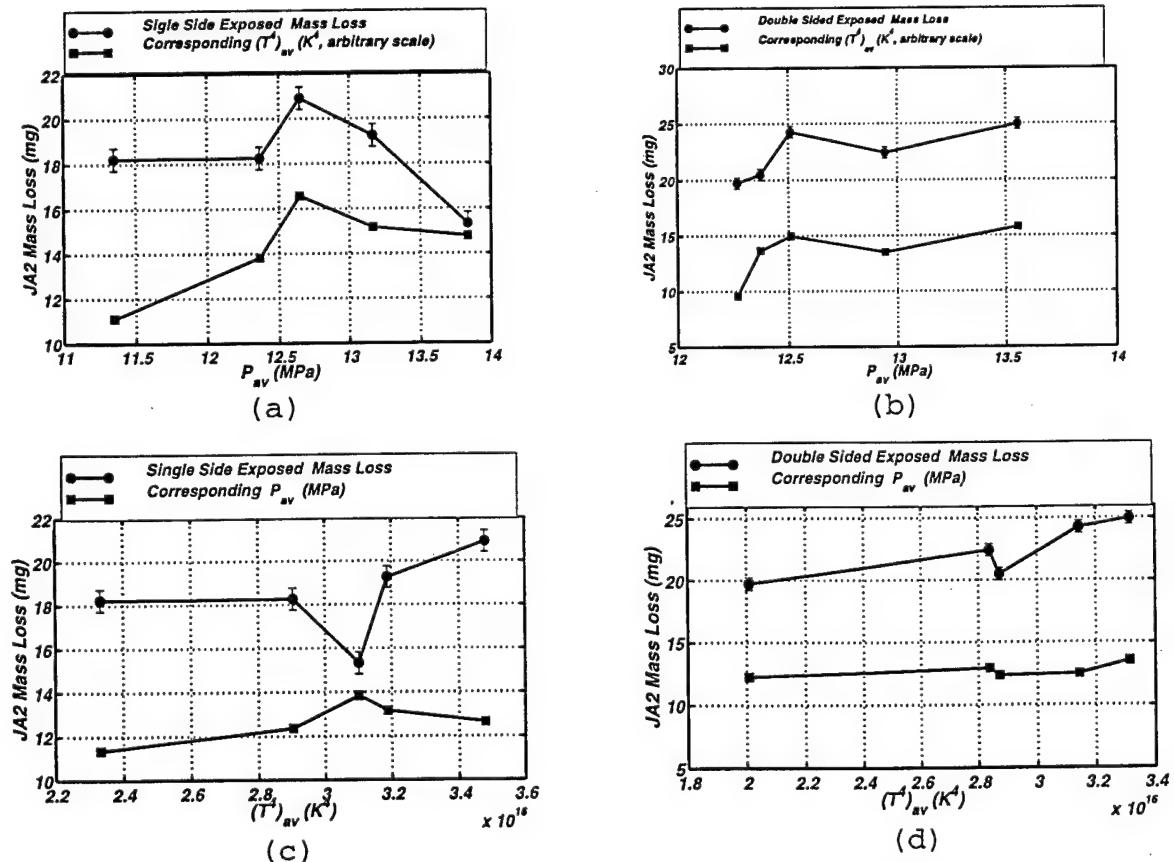

Fig. 21 Measured burn rate (JA-2 mass loss for incomplete burn) versus the corresponding computed plasma parameters. Results for samples shot single-side are shown on the left graphs, and samples shot double-sided are shown on the right graphs.

18

In Fig. 21(a,b), JA-2 mass loss and the corresponding $(T^4)_{av}$ are plotted versus the computed Pav, while $(T^4)_{av}$ and Pav have interchanged in Fig. 21(c,d). Considering each set of data separately, the following features can be recognized:

- For single side exposed samples, the data points of the propellant mass loss apparently follow the shape of $(T^4)_{av}$, as it is obvious in Fig. 21(a), while the pressure shows a pseudo negative effect on the mass loss. This negative effect can be seen clearly in Fig. 21(c).
- For double-sided exposed samples, gasification rate still follows the shape of the average radiant temperature as in Fig. 21(b) and also follows the shape of the average pressure as can be seen from Fig. 21(d). The pressure is no longer show the pseudo negative effect shown with the single-side exposed samples. The appearance of negative pressure effect with fresh samples and the disappearance of such negative effect with exposed samples suggests the following interpretation: The pseudo negative effect observed with the single-side exposed samples may be nothing but reduction of the radiation role due to shielding, effect which may be caused due to the build up of dense particle population in the moderator section. This interpretation is adopted here for the following reasons:

    1) it does not violate the well known behavior of increasing burn rate with increased pressure in conventional ignition, where the radiation role does not exist; and
    2) this effect does not appear in the double-sided exposed sample behavior where permanent in-depth radiation effects from the first exposure, likely, do exist and as a result the shielding of radiation does not have the same important role. It is too early for the currently available number of data points to correlate the gasification rate of JA-2 to plasma temperature and pressure by semi-empirical correlation.

The above investigation may be summarized as follows:
- Gasification rate of JA-2 propellant shows strong dependence on plasma radiation and a negative pressure dependence on the plasma pressure for single-side exposed samples.
- For double-sided exposed samples, the JA-2 gasification rate maintains its dependence on the plasma average radiant temperature and shows a positive pressure effect in the same time.
- JA-2 mass loss for double-sided exposed sample always shows values higher than the corresponding single-side exposed samples. This finding simply indicates that there is another effect, different from conditioning effect or surface kinetics, that can affect the gasification rate of JA2 solid propellant. This is likely the effect of in-depth interaction7. Further investigation of the in-depth interaction will be conducted.

SEM micrographs of JA-2 exposed samples show erosion and in-depth changes of the propellant grain. Unexposed and exposed JA-2 samples were analyzed using Scanning Electron Microscopy (SEM). The only difficulty is sample vaporization from the heat flux of the electron beam used to scan the surface, especially at high beam currents and high magnifications (>60% max. current and >IkX magnification). To obtain reasonable images, beam current was reduced to 45% and the JA-2 samples were sputter-coated with gold layer approx. 200nm thick. Fig. 22(a) is a 35X image of un-exposed sample, surface view, which displays general un-exposed surface characteristics. The holes (perforations) are visible and give indication of size and spacing of the surface features. Fig. 22(b), is a micrograph of the exposed sample where ET plasma was directly incident on the JA-2 sample. Surface erosion is evident, as well as development of microcracks. Fig. 23(a) is a 500X depth view of unexposed cut-away sample that looks into one of the sample's perforation. The irregular particles are observed along the entire length of the hole, as are the striations in the background. Fig. 23(b) is a cut-away of exposed sample, which displays the inner surface of a hole in the sample after exposure to plasma. It is clear that the plasma, either partially or fully, flows through the perforations and inner surface conditioning took place with evidence of erosion and microcracks. Surface features of exposed samples resembles features of

ablating surfaces under radiation heat flux. Fig. 24(a) is a 500X surface view of un-exposed sample, looking at top of the sample, where surface features are not too different from the unexposed depth image at same magnification. The exposed sample, Fig. 24(b), where surface modification is evident and cracks are developed, possibly due to the large plasma pressure on the surface. Fig. 25(a) is a 100X surface view of exposed sample, exposed surface is at bottom of the micrograph, where erosion and pitting is clear. Such erosion/pitting was not observed neither on the unexposed depth images nor the cut-edge of the exposed sample. A close-up (500X) of the plasma-exposed edge of the exposed depth sample is shown in Fig. 25(b), where erosion and pitting near the surface is evident (bottom of image). Analysis of exposed samples indicates ablative behavior similar to that observed on solid materials exposed to radiation heat flux from electrothermal plasmas [43-45]. It is quite important to note that such preliminary SEM analysis is not conclusive to whether only radiation energy is responsible for erosive burn, or additional mechanisms are involved.

| (a) | (b) |
| Un-exposed | Exposed |
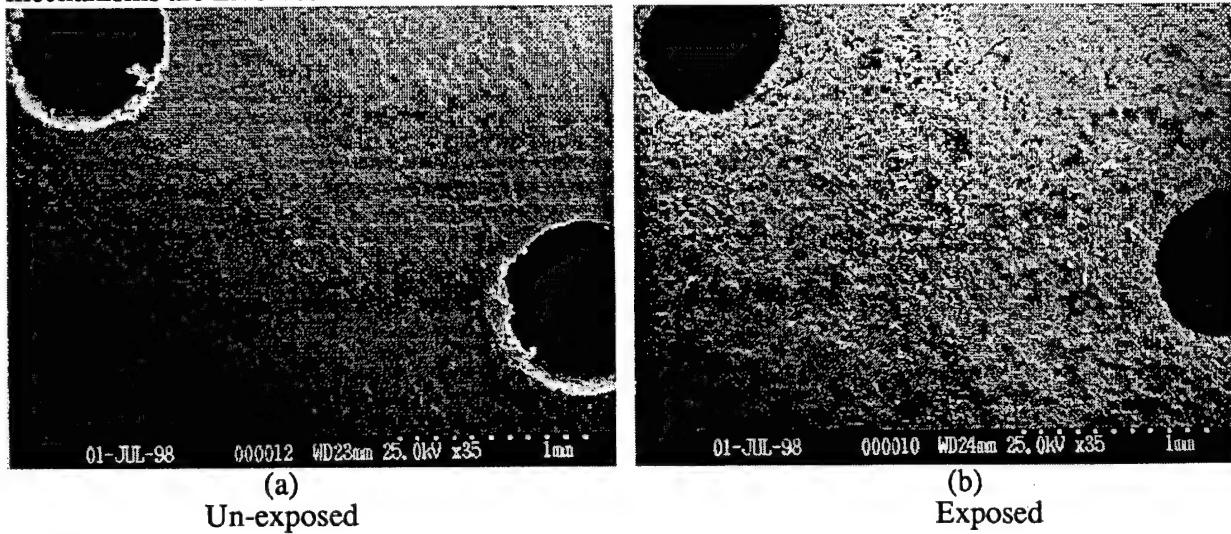
Fig. 22 SEM surface view of unexposed sample (a), and exposed sample (b) showing evidence of surface erosion.

| (a) | (b) |
| Un-exposed | Exposed |
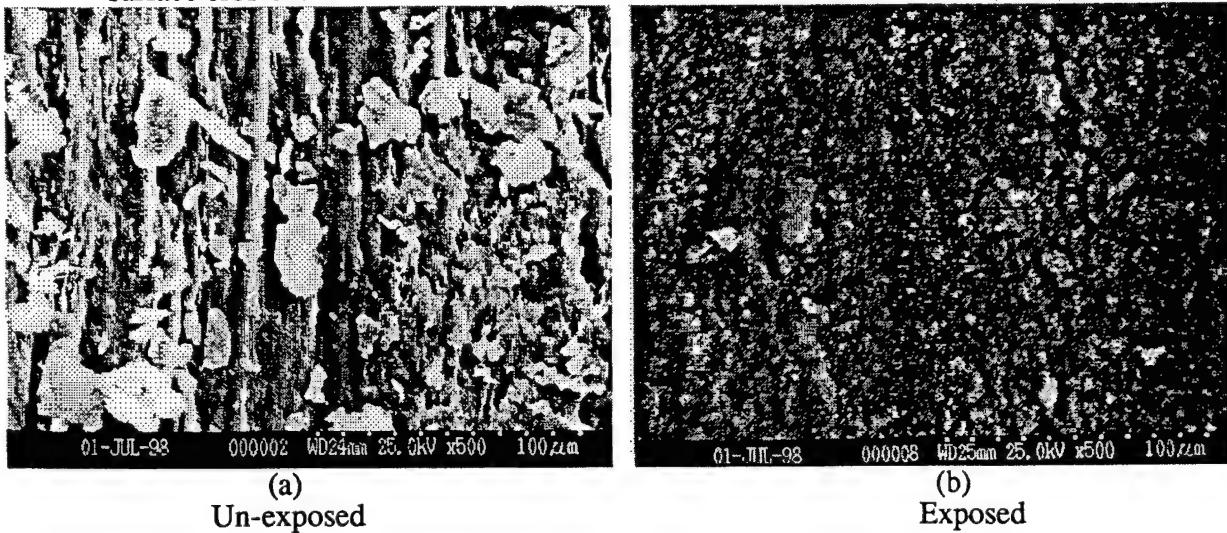
Fig. 23 SEM depth view of unexposed cut-away sample that looks into one of the perforation (a) showing irregularity and striations in the background; and exposed sample (b) showing the inner surface of a hole in the sample after exposure to plasma.

<div style="text-align:center">(a)
Un-exposed</div>

<div style="text-align:center">(b)
Exposed</div>
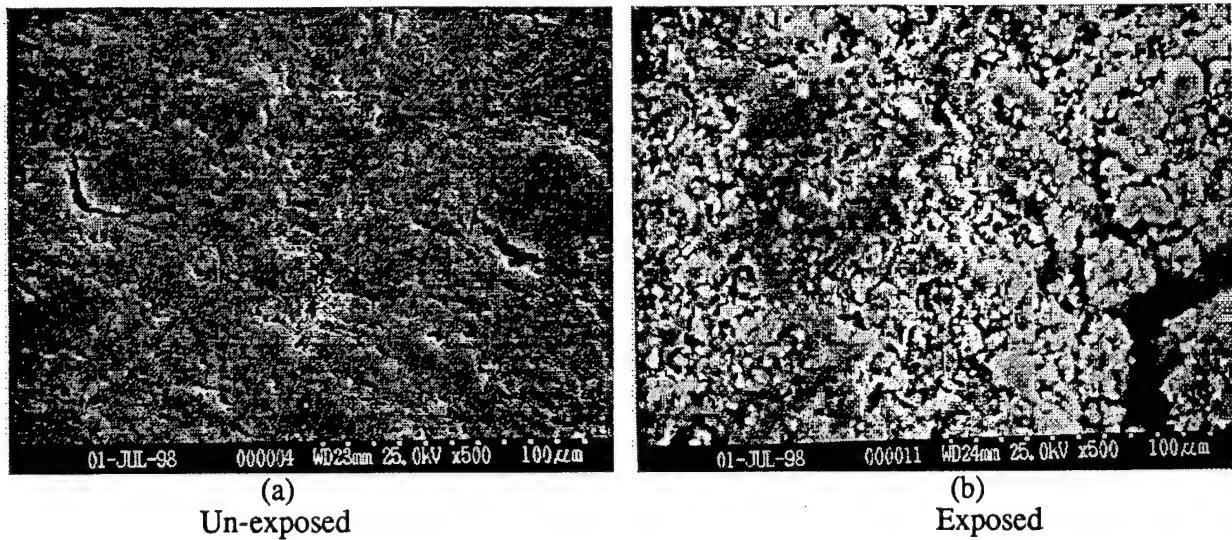
Fig. 24 SEM surface view of un-exposed (a), and exposed (b) sample showing evidence of surface modification and formation of cracks in plasma-exposed JA2 samples

<div style="text-align:center">(a)
Exposed</div>

<div style="text-align:center">(b)
Exposed</div>
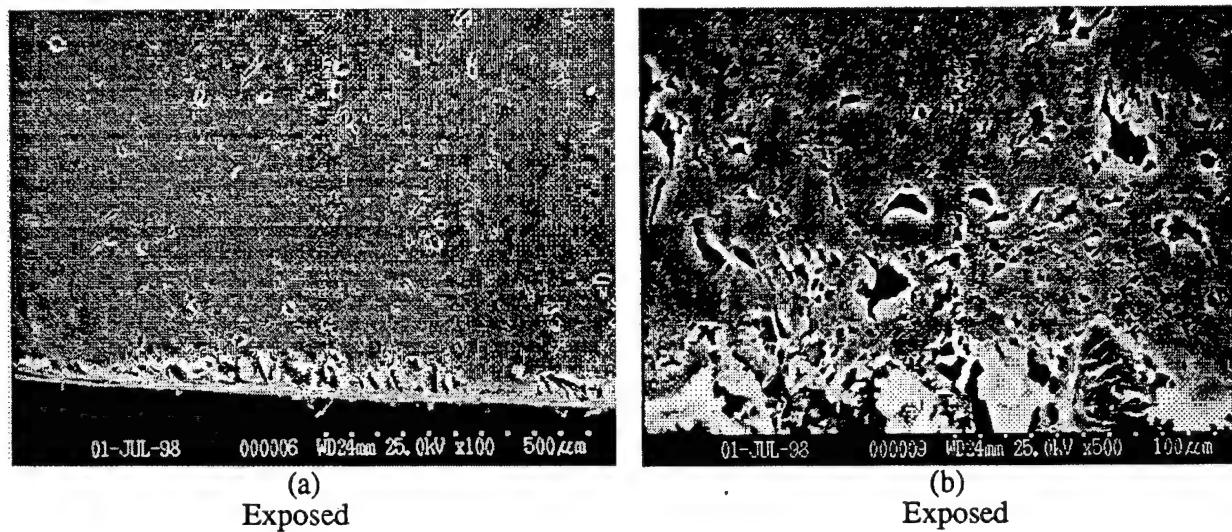
Fig. 25 SEM surface view of plasma-exposed sample (a) 100X, (b) 500X, showing surface erosion and pitting. Exposed surface is at the bottom of the image

VI. OPTICAL EMISSION SPECTROSCOPY: PLASMA PARAMETERS AND VAPOR SHIELD

As mentioned in the previous sections, Optical emission spectroscopy (OES) is used to estimate plasma composition, density, and temperature. OES is performed using a Tracor Northern TN-6500 Optical Multichannel Analyzer (OMA) system, which consists of a TN-6049A spectrograph with a 512-pixel TN-6113 photodiode array detector and the associated computer system. The OMA records one time-integrated spectrum over the length of the discharge. Single quartz optical fibers are used to view the plasma and bring the spectral output to the OMA. Visible emission is corrected for relative detector responsivity and geometric grating effects. The OMA is

calibrated for wavelength using reference lamps but is not absolutely calibrated for intensity. All spectra discussed in this paper were taken using 600 groove per mm grating and a resolution of ±0.5 nm. Plasma temperatures and densities are estimated using the relative intensities and widths of neutral copper lines in the 500 to 580 nm spectral region. Copper is a constituent of the cathode material (HD-17 tungsten alloy), and is present in the plasma as a result of electrode erosion. The temperatures are estimated by doing Boltzmann plots of the relative intensities. Densities are estimated by measuring the broadening of the lines by the Stark effect.

Addition estimates of the temperatures and densities for some shots were analyzed by observing the C_2 Swan Bands ($d^3\Pi$-a^3) that are observed in the 420 to 570 nm spectral region. These spectra are routinely seen at 90^0 viewing geometry for firings using the Lexan insulator. The data were compared with synthetic spectra calculated using the UVCODE molecular spectra-radiative transport code developed by Berk, et al. [41]. Since it was developed to treat non-equilibrium radiation processes, this code allows the specification of separate temperatures for translational, rotational, vibrational and electronic levels of both the upper and lower states of radiating molecules. Thermodynamic equilibrium is assumed for the radiation calculation and therefore, equal temperatures for all levels. Calculations were made at 15 cm^{-1} spectral resolution, equivalent to the experimental resolution of 0.5 nm. Pressure, gas temperature, and C_2 column density (density times path length, number/m^2) were varied to obtain a match between the data and predictions. Total pressure was not a critical parameter, since the spectral resolution was rather low. The relative intensities of the band heads in the $\Delta v = -1$ band progression, 545 to 565 nm, were used to determine the overall temperature, while the ratio of intensities of the (0,1) bandhead at 563.6 nm to (0,0) bandhead at 516.5 nm was a good indicator of C_2 density.

The set of experiments conducted on the PIPE device were designed to measure the burn rates of JA-2 solid propellant as a function of plasma injection angle. The results have shown an increased burn rate with increased angle of injection, such that a maximum burn rate is achieved when plasma is injected normal (90^0) to the surface of the propellant. Optical emission spectroscopy measurements were taken during some of the shots with all shots having the same input energy (5.1 kJ ± 5%). Fiber optics were situated in two places, one closer to the plasma source and the second at the rear edge of the propellant sample. A comparison between two spectra, one at the source exit (P089) and one at the propellant's rear edge (P092), is shown in Fig. 26. Both spectra were taken at the same angle of inclination of the propellant sample (15^0 from source axis). Spectra are indicative of a continuum with superimposed atomic copper lines and C_2 Swan Bands. It is clear that the relative intensity of copper lines (between 500 and 530 nm) closer to the source is about a factor of 2.5 higher than that at the rear edge of the propellant sample. Farther away, at the rear edge of the propellant, the plasma is expected to be cooler and more neutral species would mix at the surface of the propellant.
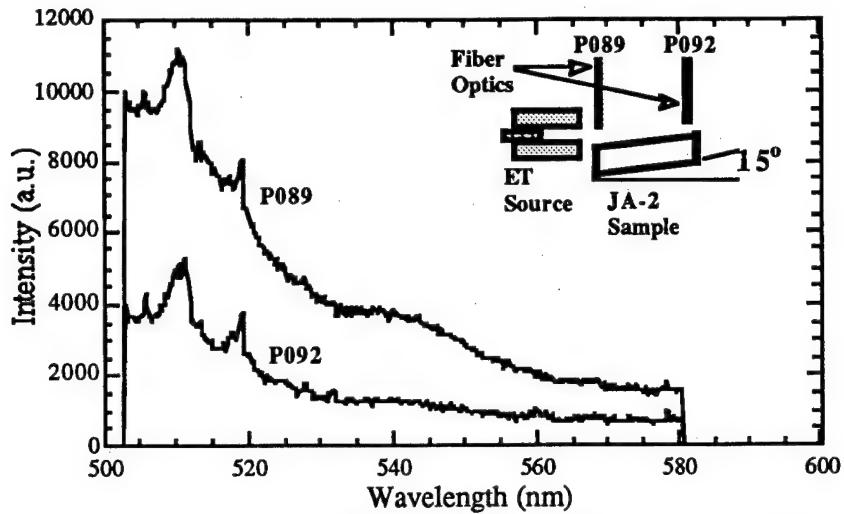
Fig. 26 Optical emission spectra taken during plasma injection into JA-2 propellant (shots # P089 and P092). Propellant sample is oriented 15° from the axis of the source. Shot P089 spectrum is obtained with the fiber optics looking to the surface of the propellant close to the source exit, while shot P092 spectrum is obtained with the fiber optics placed at the rear of the propellant.

Another comparison is shown in Fig. 27, where shot P089 spectrum is compared to that of shot P091. The difference is that shot P091 spectrum is taken for an inclination angle of 0^0. It is clear that the relative intensity is approximately the same as that of shot P092 (15^0) except that copper lines are sharper. A comparison between spectra taken at the rear edge of the propellant, at different plasma injection angles, is shown in Fig. 28 for shots P091 (0^0), P092 (15^0), P093 (30^0) and P094 (45^0). Fig. 5 compares shots P108 (60^0) and P111 (90^0). The general trend shows an increased relative intensity as the angle of injection increases up to 30^0, then decreases thereafter at 45^0 and 60^0, followed by an increase at 90^0.
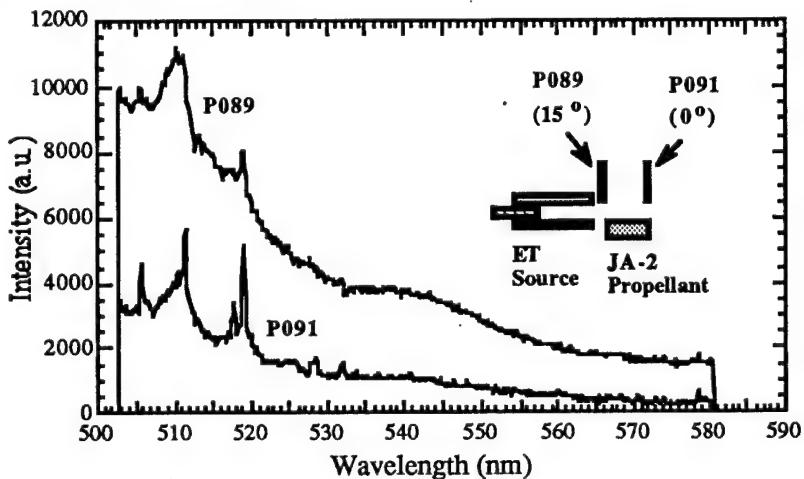
Fig. 27 Comparison between optical emission spectra taken during shots # P089 (15°, near source) and shot P091 (0°, near sample rear edge).
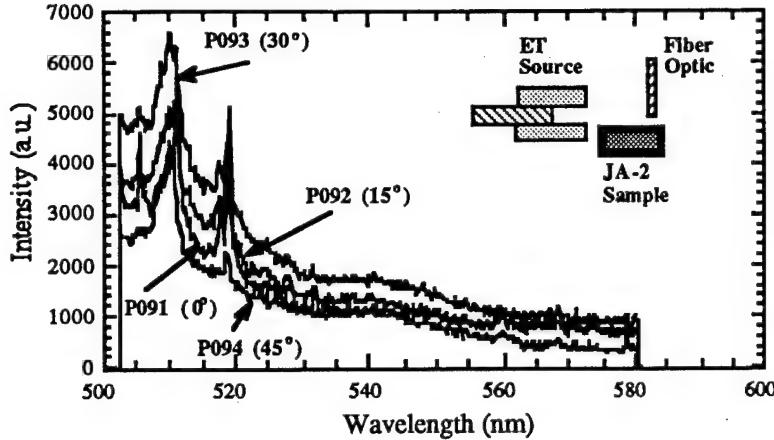
Fig. 28 Optical emission spectra taken during shots P091 (0°), P092 (15°), P093 (30°) and P094 (45°), showing the change in the relative intensity as the angle of injection changes.

It is also noticeable that CO_2 molecular and copper atomic components have nearly broadened into the continuum, as seen in Fig. 29. Total integrated intensities of the spectra as a function of the injection angle are shown in Fig. 30. The integrated intensity with increased angle of injection is only weakly correlated to the increased burn rate with angle in that the intensity increases up to 30°, but decreases at 45° and 60° and then increases substantially at 90°. A possible explanation is that at 45° and greater, the vapor shield plasma is optically thicker because of the increased burn rate and the increase in the neutral constituents at the interface.
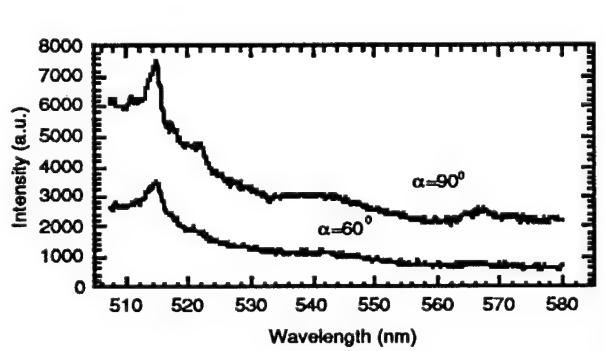
Fig. 29 Optical emission spectra taken during shots P108 (60°) and P111 (90°), showing the lack of CO_2 molecular features and the change in the relative intensity as the angle of injection changes.
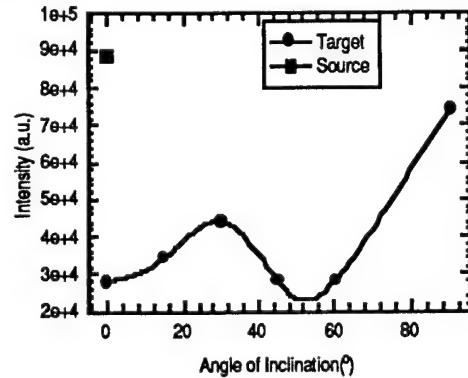
Fig. 30 Change in integrated light emission as a function of the inclination angle.

Fig. 31 shows plasma temperature, as calculated from spectroscopy measurements, where the plasma temperature at the surface of propellant for the 0° injection angle is 20% higher (1.2 eV) than that of the source (1.0 eV), which may be attributed to the combustion of the propellant. As the injection angle increases, the plasma temperature observed decreases because the burn rate increases and the vapor plasma becomes thicker and expands against the surface of the propellant. At 45°, 60°, and 90°, the plasma temperature at the rear edge of the propellant sample is 0.8 eV, about 20% less than that of the source. The plasma density, as shown in Fig. 32, follows the same trend and decreases with increased angle of injection except at 90°, where it increases substantially.

Although the burn rate increases, and more mass is evolving from the surface, ionization goes down (as the temperature decreases), which results in increased neutral constituents and a lower plasma density. At 90^0, the burn rate increases substantially as the target receives the full kinetic energy of the plasma. The observed increases in plasma density and integrated emission are the result of this increased mass evolution.
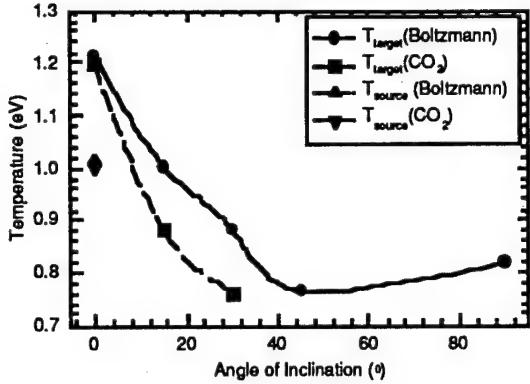
Fig. 31 Change in plasma temperate at the surface of the propellant sample as a function of the angle of injection, as calculated using a Boltzmann plot of neutral copper lines and a match of CO_2 emission predictions with the data. The source temperature is also shown.
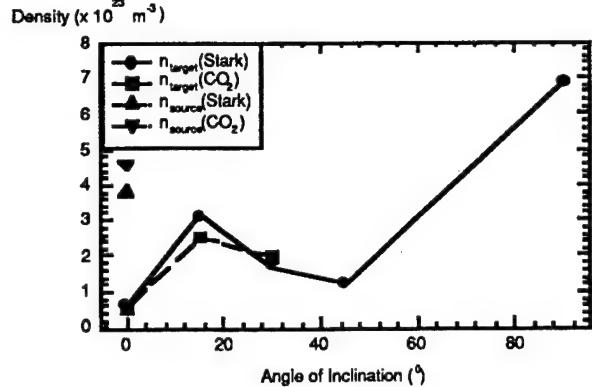
Fig. 32 Change in plasma density at the surface of the propellant sample as a function of the angle of injection, as calculated from the Stark broadening of neutral copper lines and matching CO_2 emission predictions with data.

In order to assess the effectiveness of the vapor shield mechanism, and effectiveness of radiative heating on propellant's bed, plasma temperature was estimated from optical emission spectroscopy at various values of energy input to the plasma source. Fig. 33 shows measured plasma temperature as a function of input energy. Vapor shield transmission factor of 10, 20 and 30% was plotted on same graph, along with no-vapor-shield effect. Also, a calculation of equivalent temperature of a blackbody considering that all electrical energy input is transferred to radiation is also plotted. It is clear that the energy transmission factor through the vapor shield varies with increased input energy, in other words with increased radiation flux. This factor is about 30% for energy inputs up to 4 kJ, 20% for energies >4 kJ but <5kJ, and reaches 10% for energies > 6kJ. These results correlates well with previous investigations on vapor shield mechanism when injecting plasma into solid surfaces, and correlates also with code predictions. Fig. 34 is another evaluation of the vapor shield based on measured plasma temperature from spectral techniques versus calculated temperatures from source ablation. The graph shows the zones where both temperatures are equal (from spectroscopy and from ablation), showing the corresponding value of the energy transmission factor. The graph shows that vapor shield has almost no effect at lower energy inputs, about 30% in the energy range of 2-3 kJ, 20% in the energy range of 4-5 kJ and 10% in the energy range of 5-6 kJ and above. These results are in correlation to calculations of both code predictions and other results obtained on a similar experiment. Thus, it is apparent that the vapor shield mechanism limits energy transport to the propellant at higher radiation heat fluxes. However, radiative heating still a strong mechanism by which energy is transported to the propellant bed and is responsible for enhanced burn rates as seen from the decoupling experiments.
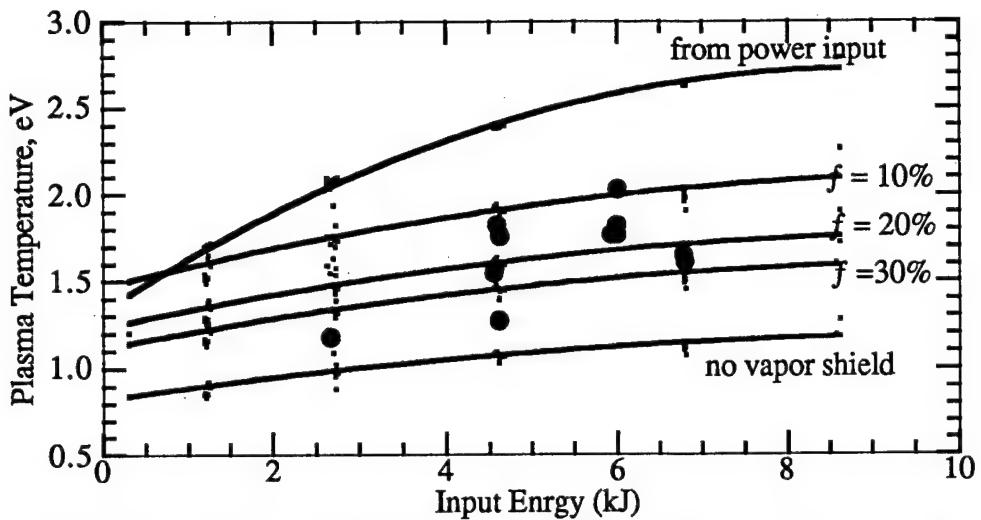
Fig. 33 Plasma temperature versus input energy to the source, showing measured temperature from optical emission spectroscopy (open diamonds) and lines of various vapor shield values. Also shown blackbody equivalent temperature obtained from power input.
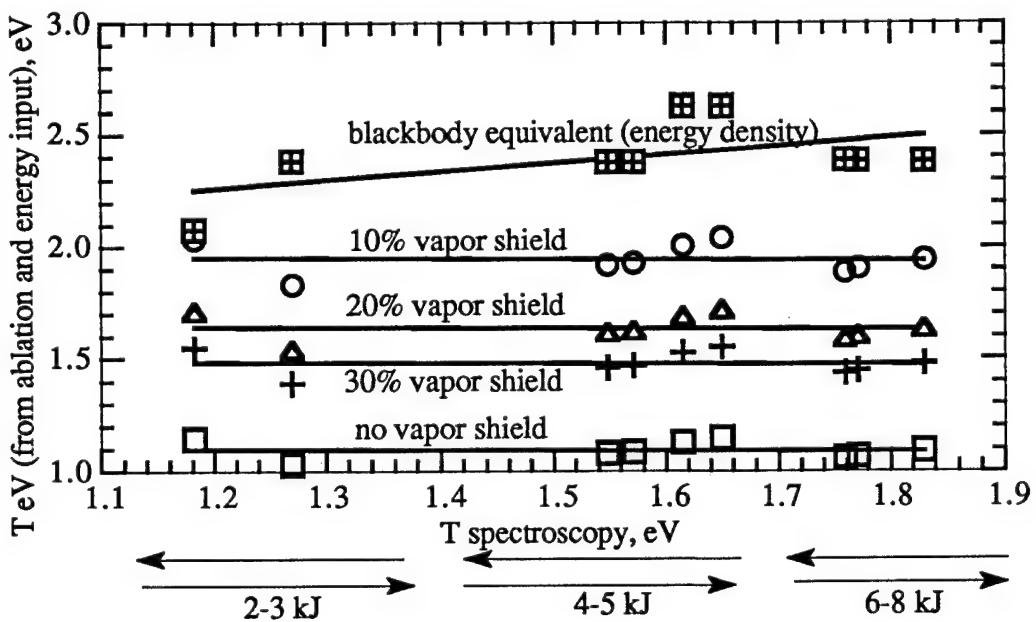
Fig. 34 Plasma temperature at source exit from optical emission spectroscopy compared to ablation with various values of the vapor shield factor, and to black-body equivalent for total energy deposition into the ET source

VII. MODELING HEAT AND CURRENT TRANSPORT IN THE PLASMA GENERATOR: "TITAN CODE"

The production of plasma discharges for injection into propellant beds for ETC applications requires the knowledge of those processes which govern the formation and propagation of the plasma. However, the diminutive size of the chamber in which these processes occur often

26

precludes implementation of diagnostic tools to directly measure plasma parameters. The TITAN code is a pseudo 2-D, time-dependent code that has been developed to model the heat and current transport in a high-density, low-temperature plasma enclosed within a cylindrical capillary. The transport of heat through radiative and thermal conduction in the radial direction, convection in the axial direction, and the distribution of current within the plasma is determined by solving energy, mass, and momentum conservation equations and the uncoupled form of Maxwell's equations. Non-ideal effects on parameters such as electrical conductivity and plasma density are also considered. In addition to the parameters noted above, for a given input current profile the code predicts gun voltage, pressure and velocity distributions as well as parameters such as thermal conductivity, internal energy, and the average ionization state of the plasma. Traditionally, the fluid characteristics of electrothermal plasma sources are described using 1-D models, which focus solely on the axial flow of ablated material through the source section of an electrothermal plasma source or through the barrel of an electrothermal launcher[9,19,20,26]. However, these models neglect transport processes such as radial heat transport and variation of current density which only a 2-D model is able to treat. A 1-D axial fluid dynamic model is solved using a two-step time advancement scheme to obtain bulk axial properties. These properties are substituted into a pseudo 2-D heat and current transport model, which solves an energy equation and the uncoupled form of Maxwell's equations using Newton's method. The plasma equation of state and transport properties used in these models include various non-ideal effects.

Plasma state and transport properties

To adequately describe the fluid properties of a non-ideal plasma, realistic models of the plasma state and transport properties are necessary. To determine the composition of a non-ideal plasma with m ionization states, m+2 equations are required; one equation for each ionization state, and two for the neutral atom and electron densities. This may be accomplished by solving a Saha equation for each of the ionization states, solving the equation of state, and assuming plasma quasi-neutrality. The quasi-neutrality assumption is given by:

$$n_e = \sum_{i=1}^{i_{max}} i\, n_i$$

where i represents the charge state of each ion group, n_i represents the number density of species i, and n_e represents the electron number density. The Saha equation describes the ionization state of a plasma at local thermodynamic equilibrium (LTE) and is given by [36]:

$$\frac{n_e\, n_{i+1}}{n_i} = 2\frac{g_{i+1}}{g_i}\left(\frac{2\,\pi\,m_e\,kT}{h^2}\right)^{3/2} \exp\left(-\frac{E_i - \Delta E_i}{kT}\right)$$

where i is the charge state of the plasma species, g_i is the degeneracy of the ith electron excitation level, and E_i is the ionization potential of the ith charge state. The correction term ΔE_i is given by :

$$\Delta E_i = \frac{Ze^2}{4\,\pi\,\varepsilon_o\,\lambda_D}$$

where Z=1 for the ionization of neutral particles, Z=2 for the ionization of singly charged particles, etc., and λ_D is the Debye length. The assumption of LTE is satisfied in general for low-temperature, high-density plasmas (T~1-3eV, n~ 10^{24}-10^{27} m^{-3}). In addition to the Saha equation and the quasi-neutrality assumption, the plasma equation of state is used and is given by [36]:

$kT\sum_{j} n_j = P + \Delta P$, where the summation is over all plasma constituents. The correction term to

plasma pressures is due to long-range Coulomb forces and is given by: $\Delta P = \dfrac{kT}{24\,\pi\,\lambda_D^3}$.

27

The corrections to the pressure in the equation of state and to the ionization potential in the Saha equation are consequences of Debye-Huckel theory. As plasma density and pressure increase, the Debye radius shrinks as $\lambda_D \sim n^{-1/2}$. Therefore, the effects of the Debye shielding decrease and long range Coulomb forces gain significance. This effectively lowers the ionization potential because fewer charged particles are shielded from striking the outer electron shells. Thus, incident particles have a greater chance of ionizing the atoms. The electrical conductivity of a partially ionized, collisional plasma may be obtained by considering contributions from both electron-ion and electron-neutral collisions [46-48]:

$$\sigma = \frac{n_e e^2}{m_e(\bar{v}_{eo} + \bar{v}_{ei})}$$

where $\bar{v}_{eo}$ is the electron-neutral collision frequency and $\bar{v}_{ei}$ is the electron-ion collision frequency. The electron-ion collision frequency is taken from the Zollweg-Liebermann model for non-ideal plasma conductivity. This formula uses a modified form of the Coulomb logarithm to account for non-ideal effects and is given by [46-50]:

$$\bar{v}_{ei} = \frac{38 Z_{eff} \ln(1 + 1.4 \Lambda_m^2)^{1/2}}{\gamma_e m_e T^{3/2}}$$

where Z_{eff} is the effective charge state, γ_e is a correction factor for electron-electron collisions [49], and Λ_m is the modified Coulomb parameter. Plasma viscosity may be defined as the sum of the partial viscosity of the neutral atoms and the ions such that $\mu = \mu_a + \mu_i$ [18,19]. Assuming that collisions are induced mainly by electrons, the thermal conductivity may be determined as a function of electron number density and collision frequency [51]:

$$\lambda_c = \frac{2.4}{1 + \bar{v}_{ei}/\sqrt{2}\bar{v}_{eH}} \frac{k^2 n_e T}{m_e \bar{v}_{eH}}$$

where $\bar{v}_{eH}$ is the net electron-heavy particle collision frequency given by $\bar{v}_{eH} = \bar{v}_{eo} + \bar{v}_{ei}$. A diffusion approximation to radiation transport within a plasma may be used for plasmas in local thermodynamic equilibrium, as the assumptions which govern the diffusion approximation (small temperature gradients and an optically thick plasma) are satisfied under the LTE assumption [52]. This diffusion approach employs a thermal conductivity-like term multiplied by the gradient in temperature to obtain a radiation flux. This coefficient of radiation heat conduction is given by:

$$\lambda_r = \frac{16}{3} \sigma_s \ell T^3$$

where (σ_s is the Stefan-Boltzmann constant and ℓ is the radiation mean free path. In multiply ionized plasmas, the radiation mean free path may be expressed as [52]:

$$\ell = 1.74 \frac{3\sqrt{3}}{16\pi^2} \frac{c(kT)^2}{h^2 e^6} \frac{(2\pi m_e kT)^{3/2}}{n_p^2 \bar{Z}(\bar{Z}+1)^2}$$

where n_p is the plasma number density and $\bar{Z}$ is the average ionization state.

The 1-D, Time-Dependent Axial Fluid Dynamics Model

The bulk plasma parameters may be determined by solving an axial set of conservation equations. A discretized form for the mass conservation equation may be obtained by integrating the conservative form of the mass conservation equation over a finite volume around an axial node such that:

28

$$\int_{V_j} \frac{\partial \rho}{\partial t} dV + \int_{S_j} \rho \vec{v}.\vec{n} \, dS = (\dot{m}_{abl})_j$$

where j refers to the jth axial node, and V_j and S_j are the volume and normal surface area at the jth node. The $(\dot{m}_{abl})_j$ term refers to the mass ablation rate from the ablating liner, or sleeve. Assuming the plasma-sleeve boundary is maintained at the vaporization temperature of the sleeve material, the mass ablated from the sleeve may be expressed in terms of the difference between the energy deposited to the wall due to black-body radiation and the energy transferred to the sleeve through conduction. The momentum equation with frictional terms may be written for axial flow thus:

$$\rho \frac{\partial v}{\partial t} + \rho \, v \frac{\partial v}{\partial t} = -\frac{\partial P}{\partial z} - \frac{F \, \rho \, v^2}{D \, 2} + \dot{\rho}_{abl} \, v_{abl}$$

where F is the friction factor and D is the sleeve diameter. For a Reynolds number below 2500, the friction factor for laminar flow is given by $F = 64/R_e$. For Reynolds numbers above 2500, the friction factor is given by the Colebrook formula [53]:

$$\frac{1}{\sqrt{F}} = 1.14 - 2.01 \, log_{10}\left(\frac{\varepsilon}{D} + \frac{9.35}{R_e\sqrt{F}}\right)$$

where ε is the roughness of the pipe. The third term on the right-hand side of the momentum equation represents the momentum flux due to ablated material. The term $\dot{\rho}_{abl}$ is given by the mass ablation rate divided by the volume into which it is ablated. The ablation velocity is given by:

$$v_{abl} = \frac{\dot{m}_{abl}}{\rho_{vap} \, A_w}$$

where ρ_{vap} is the density evaluated at the vaporization temperature and A_w is the wall surface area from which the material is ablated.

The integral form of the energy conservation equation is given by:

$$\int_{V_j} \frac{\partial \rho \, u}{\partial t} dV + \int_{S_j} \rho \, u\vec{v}.\vec{n} \, dS = -P_j \int_{S_j} \vec{v}.\vec{n} \, dS + \int_{V_j} \dot{q}''' dV - \int_{S_j} \dot{q}''_{bb} \, dS + (\dot{m}_{abl}h_{abl})_j + \int_{S_j} \lambda_s \vec{\nabla}T.\vec{n} \, dS$$

The second term on the right-hand side is the volumetric heat generation rate given by joule heating and the third term on the right-hand side signifies losses due to blackbody radiation. The fourth term refers to the addition of ablated material into the plasma and the final term refers to losses due to conduction to the wall. In the axial model, the volumetric heat generation rate may be expressed by $\dot{q}''' = J_{tot}^2 / \, \sigma$, where J_{tot} is the current density ($J_{tot} = I_{tot}/\pi R^2$), R is the plasma radius and σ is the electrical conductivity. The heat flux due to blackbody radiation emitted from the plasma is given by: $\dot{q}''_{bb} = \sigma_s(T_{plasma}^4 - T_{vap}^4)$, where σ_S is the Stefan-Boltzmann constant and T_{plasma} is the temperature of the plasma edge. An energy balance at the plasma-sleeve interface reveals that the losses from the plasma due to radiation and conduction to the wall are balanced by the gain of ablated material. Therefore, a jump boundary condition may be imposed at the plasma edge which defines the ablation rate:

$$\dot{m}_{abl} = \frac{A_w}{H_{sub}}\left(\dot{q}''_{bb} + \lambda \frac{\partial T_s}{\partial r}\bigg|_{R_{plasma}}\right)$$

where H_{sub} is the heat of sublimation and λ_s is the thermal conductivity of the wall "sleeve" material. The conduction term is determined by solving a heat conduction equation in the surrounding sleeve and insulator. This equation is given for a 1-D radial geometry by:

$$\frac{\rho_x C_{p_x}}{\lambda_x} \frac{\partial T}{\partial t} = \frac{1}{r} \frac{\partial}{\partial r}\left(r \frac{\partial T}{\partial r}\right)$$

where the subscript x refers to material properties of either the sleeve or the surrounding insulator. The temperature of the inner boundary of the sleeve is maintained at the vaporization temperature. The interface condition for the sleeve-insulator interface is continuity of temperature and heat flux, and the outer boundary of the insulator is maintained at ambient temperature. The ablation enthalpy in the energy equation is given by $h_{abl} = u_{vap} + (P/\rho_{vap})$, where u_{vap} and ρ_{vap} are the internal energy and density of the plasma evaluated at the vaporization temperature, respectively. The internal energy is related to the temperature by: $U = 1.5kT(1 + \overline{Z}) + \overline{I} + H_{sub}$, where $\overline{Z}$ is the average ionization state and $\overline{I}$ is the effective ionization energy, and $\overline{Z}$ is given by: $\overline{Z} = n_e / \sum_{i=0}^{i_{max}} n_i$, where n_e is the electron number density and the summation is taken over all heavy particles (ions and neutrals). The effective ionization energy is given by: $\overline{I} = \sum_{i=0}^{m-1} I_i + (\overline{Z} - m) I_m$, where m is the integer value of the average ionization state. This formula is based on the assumption that the ion number densities n_m and the ionization potentials I_m are, at least macroscopically, continuous functions of the ionization state m and behave in a linear fashion between the discrete ionization potentials [52].

The numerical solution of the axial fluid dynamics model employs a two-step time advancement scheme. The first step involves a semi-implicit reduction of the conservation equations and a linearized equation of state using intermediary "new" time values for density and internal energy. These intermediary values are not carried to the next time but are only used in the reduction of the conservation equations. The new time pressures and velocities are then calculated from these reduced forms. New time density and internal energy are determined by a second step in the time advancement scheme. By rewriting the mass and internal energy equations in terms of the new time pressure and velocity, the new time density and internal energy can be calculated. Time step size is controlled to limit the truncation error associated with the linearized form of the equation of state. Because velocities at the sleeve exit may exceed the sound speed, a choking criterion is placed at the sleeve-expansion chamber boundary. This criterion imposes a velocity boundary condition by limiting the velocity at the sleeve exit to the sound speed.

The Pseudo 2-D Heat and Current Transport Model

Given the bulk plasma parameters from the axial model at each time step, a radial energy equation may be solved at each axial node. The discretized form of the radial energy equation is obtained by integrating the conservative form of the energy conservation equation over a series of finite volumes such that:

$$\int_{V_{ij}} \frac{\partial \rho u}{\partial t} dV + \int_{S_j} \rho u \vec{v}.\vec{n} \, dS = -P_j \int_{S_j} \vec{v}.\vec{n} \, dS + \int_{V_{ij}} \dot{q}'' dV_{ij} + \int_{S_{ij}} (\lambda_c + \lambda_r) \vec{\nabla}T.\vec{n} \, dS$$

where λ_c and λ_r are the thermal and radiative conductivities, respectively. The integration is performed over a series of concentric "rings" centered upon the ith radial node and the jth axial node. Since convection and fluid work is only considered in the axial direction, their respective surface integrals are performed over the area normal to axial flow. Similarly, since conduction is

30

only considered in the radial direction, the surface integral for the conduction term is performed over the area normal to the radial direction. The outer boundary condition is determined by performing an energy balance at the plasma-sleeve interface. This results in an ablation enthalpy term, a radiative loss term, and wall conduction terms, as described in the axial model. The joule heating term in the radial model is given by $\ddot{q}'' = J^2 / \sigma$. The distribution of current within the plasma may be described in terms of the induction field by employing Maxwell's equations and Ohm's law: $\vec{\nabla} \times \vec{B} = \mu \vec{J}$, $\vec{\nabla} \times \vec{E} = -\partial \vec{B} / \partial t$ and $\vec{J} = \sigma \vec{E}$; where $\vec{E}$ is the electric field intensity. Assuming that the axial gradients of electrical conductivity and induction field are relatively small, these equations may be uncoupled in 1-D cylindrical coordinates such that [54,55]:

$$\mu\sigma \frac{\partial B}{\partial t} = \frac{\partial^2 B}{\partial t^2} + \frac{1}{r}\frac{\partial B}{\partial r} - \frac{B}{r^2} - \frac{1}{\sigma}\frac{\partial \sigma}{\partial r}\frac{\partial B}{\partial r} - \frac{B}{\sigma r}\frac{\partial \sigma}{\partial r}$$

The numerical solution of the pseudo 2-D model is obtained by discretizing the energy equation and the uncoupled Maxwell's equations. The density, pressure, and velocity at each axial position are taken from the results of the axial model. Coupling of the induction field equation to the energy equation occurs through the Joule heating term in the energy equation and the temperature dependence of the electrical conductivity in the induction field equation, producing a system of nonlinear algebraic equations which are solved simultaneously using a Newton-Raphson scheme. This scheme yields a 2-D distribution for temperature, induction field, and the various plasma transport parameters.

Code Testing and Comparison to Experimental Data

The TITAN code was run for a shot, where a copper sleeve were used to produce a metal-vapor plasma, and was insulated at both ends by ceramic end-sleeves. The maximum current for this shot was 34.84 kA over a pulse duration of 50 μs. The computed time evolution of the plasma pressure is shown in Fig. 35. As material from the wall is ablated and heated, sharp pressure gradients form within the source section, which drive the plasma into the expansion chamber. The pressure reaches a maximum at 35 μs at which point the losses due to transport of plasma into the expansion chamber exceed the gain of material through ablation. Fig. 36 shows the time evolution of the plasma density with the density profiles closely following those for pressure. Density gradients are formed as ablated material close to the sleeve exit is ejected into the expansion chamber. Plasma density reaches a maximum at 38 μs, which corresponds closely to the peak in pressure.
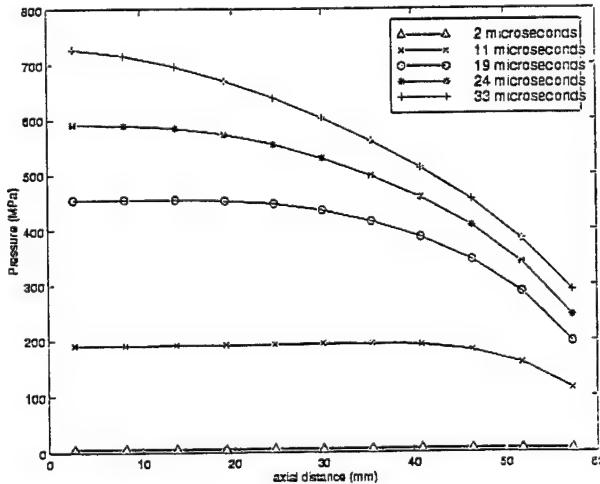

Fig. 35 Axial variation of plasma pressure   Fig. 36 Axial variation of plasma density
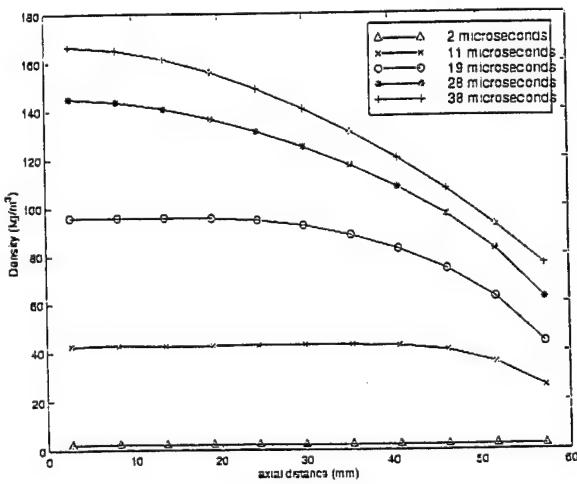
31

The time evolution of the plasma velocity is given in Fig. 37, which shows that the velocity increases rapidly until reaching a maximum at 25 μs. At this point the flow out of the sleeve is already choked and is limited by the sound speed. Material flow from the sleeve is restricted and thus the maximum pressure and density are dictated by the rate of ablation. A better indicator of the choking phenomena is illustrated in Fig. 38, where it can be seen that at 20 μs the velocity at the source exit converges to the sound speed, and is maintained through the remainder of the shot.
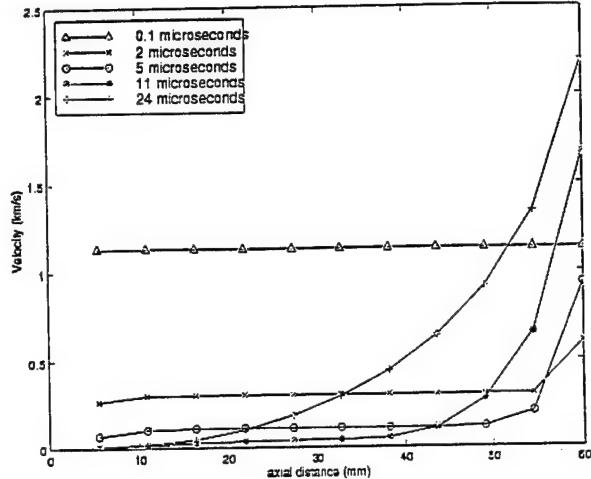

Fig. 37 Axial variation of plasma velocity
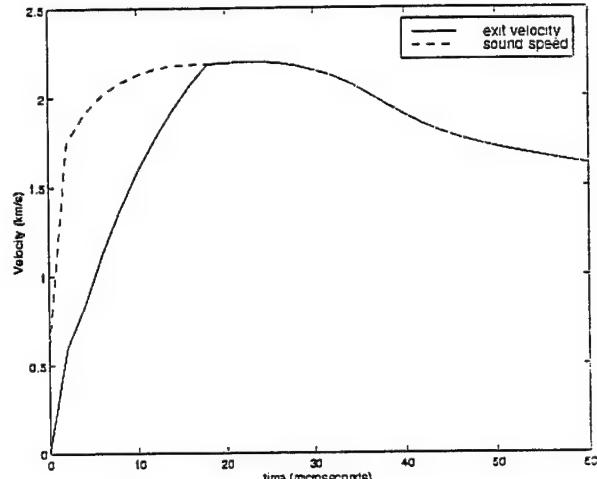
Fig. 38 Plasma exit velocity

The evolution of the plasma temperature, during and after the shot, is shown in Fig. 39. Initially the temperature remains fairly constant as the coefficient of radiation transport effectively distributes energy from joule heating. Even at a 19.7 μs, when the temperature reaches a maximum of 29,000K (2.5eV), temperature gradients exist solely at the plasma edge, where heat is lost to the sleeve. However, at 35 μs the gradients in temperature become significant. This is due to the high dependence of the radiation conductivity on plasma pressure. Thus, when the plasma pressure reaches a maximum, the radiation conductivity is the lowest, allowing large temperature gradients, particularly at the plasma edge. As the plasma begins to cool, the effects of axial convection on the plasma temperature become more evident. Comparison of the temperature distribution at 35 μs and the temperature distribution at 49 μs reveals that while the radial gradients in temperature remain relatively constant, the axial gradients in temperature increase. However, it should be noted that while the axial gradients occur over a total distance of 60 mm, the radial gradients occur over a distance of less than 2 mm. Therefore the plasma is relatively isothermal in the axial direction. Once the shot ends the losses due to convection begin decreasing, though the radial gradients in temperature remain due to cooling at the plasma-sleeve boundary. The time evolution of the current density is shown in Fig. 40, where it can be seen that the current density is similar in form to the plasma temperature. This is due to the temperature dependence of the electrical conductivity. At low temperatures the ionization rate and thus the conductivity remain small. Therefore, current will tend to flow near the plasma center where the temperature, and thus the electrical conductivity, are high. However, it can be seen that the gradients in the current density are small. This is due to the assumption that ablated material is distributed uniformly in the radial direction. Without radial gradients in density, the temperature and current density distribution will tend to be flat. Nevertheless, because of the magnitude of the current density and since it is squared to obtain the joule heating term, even small variations in the current density will significantly affect the temperature.

32
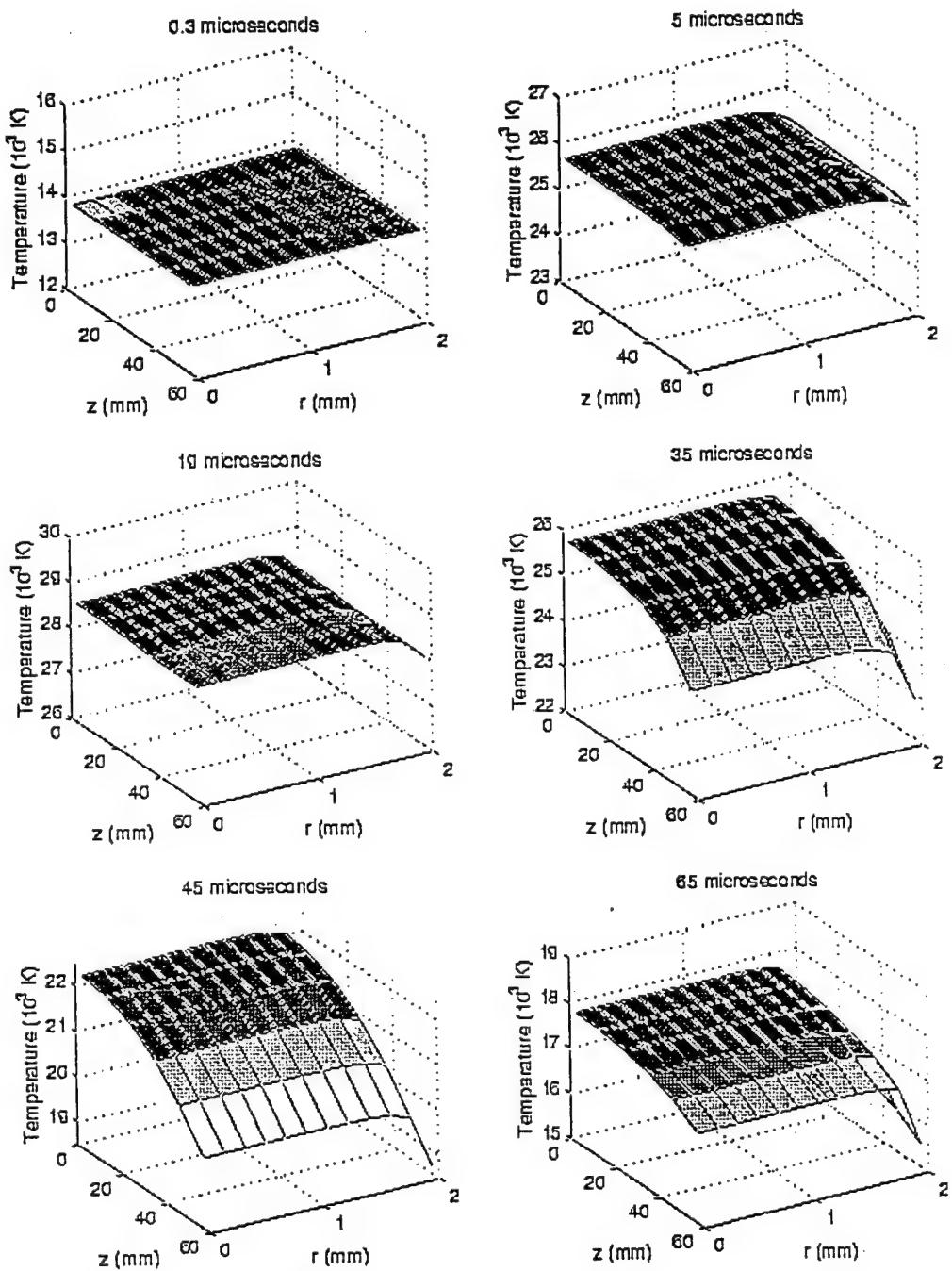
Fig. 39 Time-evolution of 2-D spatial distribution of plasma temperature variation
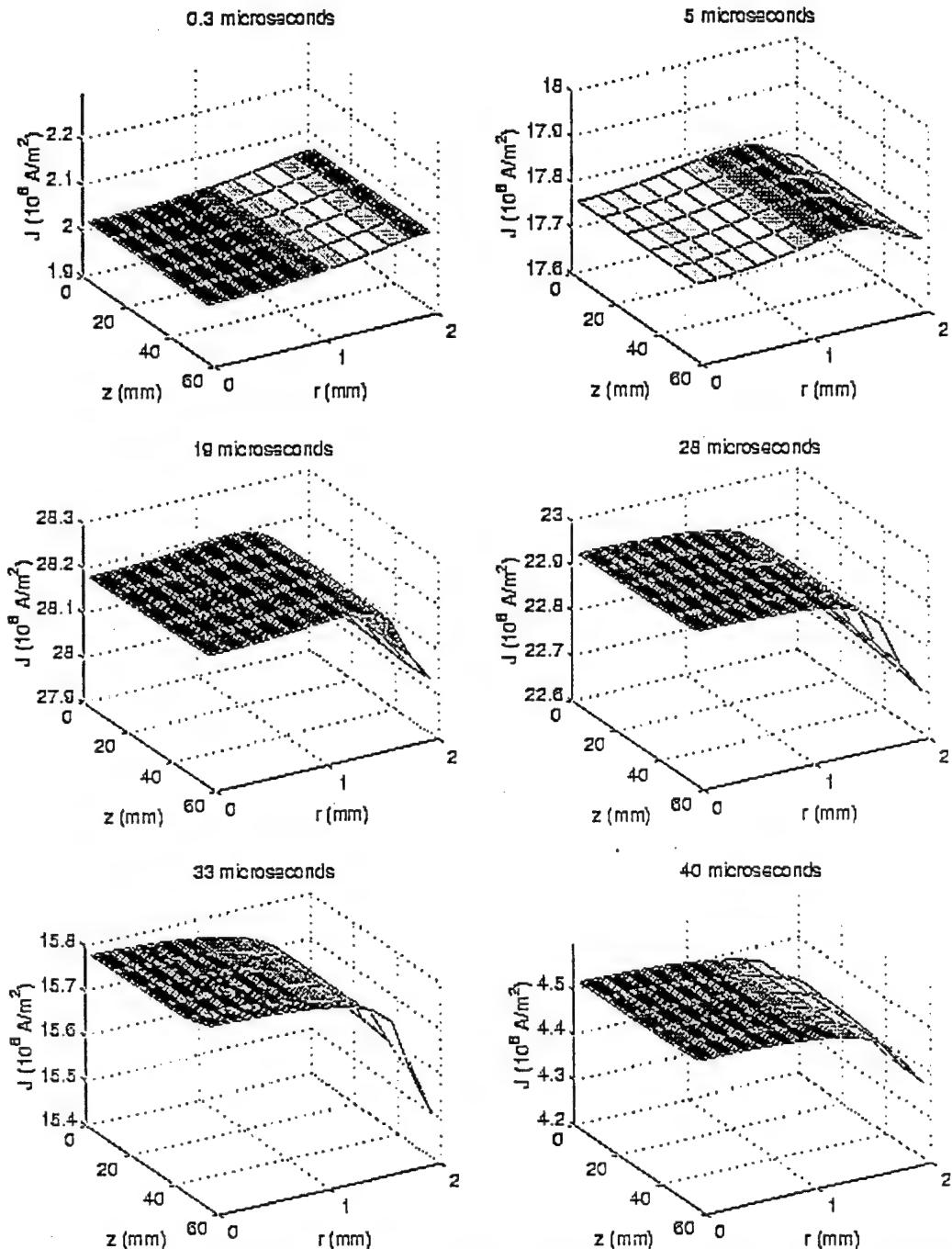
Fig. 40 Time-evolution of 2-D spatial distribution of current density variation

Comparison of code results with experimental data

The results of the TITAN code were verified by comparisons to experimental results. In addition to the discharge current, the discharge voltage across the source section is obtained via a capacitively-coupled high-voltage probe. A simple calculation has been done in TITAN to predict the voltage by assuming the source section acting like an overdamped circuit. Therefore, the voltage can be determined by Ohm's law, V=IR, from the current data and the electrical conductivity. The results of TITAN calculation and the actual measured voltage are shown in Fig. 41. While the TITAN calculated voltage reaches a peak of 5.3 kV, the actual voltage peak is 6.1 kV. Also, the voltage calculated by TITAN seems to be delayed compared to the experimentally obtained voltage. The discrepancy concerning the voltage peak can be explained by the assumption that the source acts like an overdamped circuit, while the actual voltage includes inductance terms, which are neglected in the TITAN calculation. The discrepancy concerning the time delay of the TITAN voltage occurs because the TITAN code assumes that the circuit is led by the current, when in actuality, the formation and propagation of the current is caused by the potential placed across the source section. Therefore while the actual voltage occurs slightly before the current, the calculated voltage appears slightly after the current. Fiber optics placed at the capillary exit provide spectroscopic information about the plasma. This data can be used to predict plasma temperatures at the sleeve-expansion chamber interface. For this experiment a time-averaged temperature from spectroscopic analysis of 2.27eV was calculated [35]. Results from the TITAN code predict a time-averaged temperature of 2.42eV over the length of the source. Because the plasma expands at the source exit, the temperature at the exit will tend to be lower than at a point within the source. This expansion may explain the lower average temperature from spectroscopy than calculated by TITAN. Additional benchmarking were performed by comparing TITAN predictions to measured pressure, as shown in Fig. 42, and plasma conductivity, where good agreements were obtained. The code predicted a peak pressure of 480MPa while the measured pressure was 500MPa. Code prediction of the plasma resistance was 0.1-0.15 Ω while measured resistance was 0.12 Ω. I addition, a comparison between TITAN results and MODIN (1-D, time-dependent plasma source code) predictions revealed good agreement between both codes and experimentally obtained data.
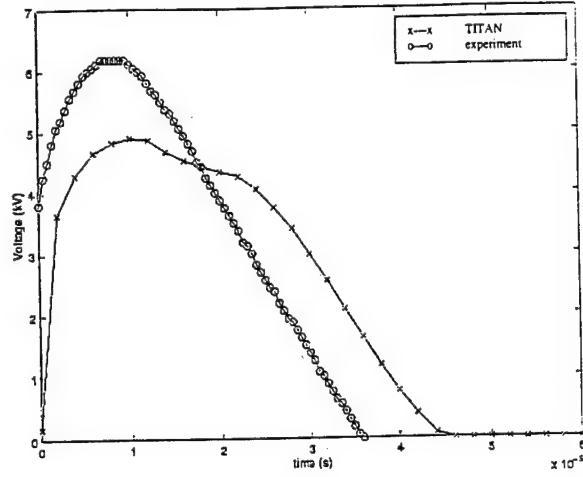

Fig. 41 Measured and calculated voltage
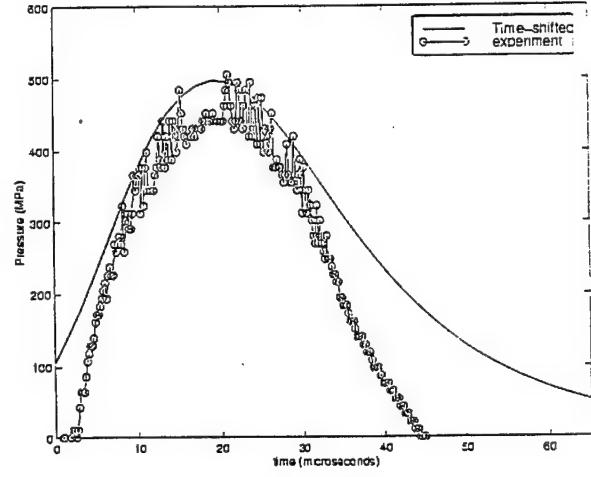
Fig. 42 Measured and calculated pressure

35

VIII. MODELING BOUNDARY-LAYER ENERGY TRANSPORT AT PLASMA-PROPELLANT INTERFACE: "TURBFIRE CODE"

The 2-D code TURBFIRE has been developed to model boundary layer plasma flow and predict mass evolution rates at plasma-propellant interfaces. This code will aid in the understanding of thermal shielding of the propellant and the effects of turbulence and radiation on energy transport to the surface. TURBFIRE allows the determination of energy transport to the surface via radiation and conduction. The system has been modeled using fluid boundary layer equations, which include a two-equation (k-ω) model for turbulence, coupled with multigroup thermal radiation transport. Both turbulence and radiation are important factors in enhancing energy transport to the surface. The code does include models of thermal conductivity and heat capacity, along with zero-gradient boundary conditions for k and ω at the freestream. A surface ablation model has also been added to investigate thermal shielding effects. This model treats ablated material as a gas at equilibrium with the bulk plasma. A combustion model is not yet included. Interaction of plasma with propellants requires detailed analysis of the energy transfer physics at the interface and the various mixing processes between combustible species and plasma particles. In addition to ablation and combustion, turbulence, radiant energy transfer and high Reynolds number are important factors in energy transport to the propellant. These effects are investigated in experimental facilities that inject electrothermal plasma into propellants for the viable application of electrothermal-chemical (ETC) guns [7,10,11,56,57]. Experimental results suggest that turbulence enhances radiation transport through the turbulent mixing of hot outer fluid with the cooler fluid near the surface. Previous models have not combined radiant energy transport with turbulent convection in a self-consistent manner. Codes such as MAGFIRE [12] have shown that radiation transport from the plasma is a dominant mechanism responsible for heating and ablating plasma facing materials, and that conduction has a small effect. Previous turbulent flow codes have also not included a true plasma model for heat capacity ($C_V = dU/dT$), which is necessary for modeling flow at plasma temperatures. To simply model important aspects of the plasma-propellant interaction, 2-D compressible flow along a flat plate is assumed [11,58]. The k-ω model [59] is used to simulate the turbulent boundary layer flow, and the fluid equations are coupled to a separate radiation transport equation.

Set of governing equations

Equation of state:
$$\overline{P} = \sum_{i=1}^{N_{species}} \overline{P}_i = \sum_{i=1}^{N \, species} \overline{n}_i k \tilde{T}(1+\overline{z}_i)$$

Equation of State for T and U:
$$\tilde{U} = \sum_{i=1}^{N_{species}} \frac{\overline{\rho}_i}{\overline{\rho}} \tilde{U}_i = \sum_{i=1}^{N_{species}} \frac{\overline{\rho}_i}{\overline{\rho}} \left[\frac{3}{2} k \tilde{T}(1+\overline{z}_i) + \overline{I}_i \right]$$

Conservation of mass:
$$\frac{\partial(\overline{\rho}\tilde{v}_x)}{\partial x} + \frac{\partial(\overline{\rho}\tilde{v}_y)}{\partial y} = 0 \quad \& \quad \frac{\partial(\overline{\rho}_a\tilde{v}_x)}{\partial x} + \frac{\partial(\overline{\rho}_a\tilde{v}_y)}{\partial y} = 0$$

Conservation of internal energy:

$$\overline{\rho}\tilde{v}_x\frac{\partial\tilde{U}}{\partial x}+\overline{\rho}\tilde{v}_y\frac{\partial\tilde{U}}{\partial y}=-P\frac{\partial\tilde{v}_x}{\partial y}+\mu\left(\frac{\partial\tilde{v}_x}{\partial y}\right)^2+\frac{\partial}{\partial y}\left[\left(\frac{\mu}{C_V}+\frac{\mu_T}{Pr_T}\right)\frac{\partial\tilde{U}}{\partial y}\right]$$

$$+\beta^*\overline{\rho}\omega k+\sum_{g=1}^{20}c\overline{\rho}\sigma_P^g\left(E_{RP}^g-E_R^g\right)$$

Radiation transport equation:
$$\frac{\partial}{\partial y}\left[K_R^g\frac{\partial\overline{E}_R^g}{\partial y}\right]=c\rho\sigma_P^g\left(\overline{E}_{RP}^g-\overline{E}_R^g\right)$$

Conservation of x-momentum:

$$\overline{\rho}\tilde{v}_x\frac{\partial\tilde{v}_x}{\partial x}+\overline{\rho}\tilde{v}_y\frac{\partial\tilde{v}_x}{\partial y}=-\frac{\partial P}{\partial x}+\frac{\partial}{\partial y}\left[\left(\mu+\mu_T\right)\frac{\partial\tilde{v}_x}{\partial y}\right]-\frac{2}{3}\frac{\partial\overline{\rho}k}{\partial x}$$

Turbulent kinetic energy (k) equation:

$$\overline{\rho}\tilde{v}_x\frac{\partial k}{\partial x}+\overline{\rho}\tilde{v}_y\frac{\partial k}{\partial y}=\mu_T\left(\frac{\partial\tilde{v}_x}{\partial y}\right)^2-\beta^*\overline{\rho}\omega k+\frac{\partial}{\partial y}\left[\left(\mu+\sigma\mu_T\right)\frac{\partial k}{\partial y}\right]$$

Turbulence specific dissipation rate (ω) equation:

$$\overline{\rho}\tilde{v}_x\frac{\partial\omega}{\partial x}+\overline{\rho}\tilde{v}_y\frac{\partial\omega}{\partial y}=\alpha\frac{\omega}{k}\mu_T\left(\frac{\partial\tilde{v}_x}{\partial y}\right)^2-\beta^*\overline{\rho}\omega^2+\frac{\partial}{\partial y}\left[\left(\mu+\sigma\mu_T\right)\frac{\partial\omega}{\partial y}\right]$$

Nomenclature
Quantities with the symbol - are time-averaged. Those with the symbol ~ are mass-weighted means

C_V	Specific heat at constant volume	v_x	Velocity parallel to the surface
f	mass fraction of ablated material	v_y	Velocity normal to the surface
k	Turbulent kinetic energy	x	direction parallel to the surface
n	number density	y	direction parallel to the surface
P	Pressure	y^+	Dimensionless distance ($=u_\tau y/\nu$)
R	Gas constant	$\overline{z}$	Average ionization
T	Temperature	ν	Viscosity
U	Internal energy	ρ	Mass density
u^+	Dimensionless velocity ($= v_x/u_\tau$)	ω	Specific dissipation rate of turbulent
u_τ	Friction velocity		kinetic energy

Boundary Conditions for the System of Equations

Variable	Inlet boundary conditions (x=0)		Wall boundary conditions (y=0)	Freestream boundary conditions (y=d)
	constant	profile		
x-velocity	$v_x = v_{x,fs}$	v_x profile	$v_x = 0$	$v_x = v_{x,fs}$
y-velocity	$v_y = 0$	v_y profile	$v_y = v_{y,abl}$	$v_y = 0$
temperature	$T = T_{fs}$	T profile	$T = T_{wall}$	$T = T_{fs}$
density	$\rho(P,T)$	$\rho(P,T)$	$\rho(P,T)$	$\rho(P,T)$
ablated species mass fraction	$x=0$	$x=0$	$x = x_{wall}$	$x=0$
turbulence KE	$k=0$	k profile	$k=0$	$dk/dy=0$
turbulence KE dissipation rate	$\omega=0$	ω profile		$d\omega/dy=0$
radiation energy density				$E_R = \sum_{g=1}^{20} E_R^g = \frac{4}{c}\sigma T^4$

Wall ablation velocity: $v_{y,abl} = \dfrac{q''}{\rho_{abl} H_{subl}}$

A new model is being incorporated to more accurately predict ablation and vapor shielding. The ablated material will be treated as a gas at equilibrium with the bulk plasma, by adding a mass conservation equation for the ablated material and modifying the equation of state. In this model, the bulk plasma and ablated material may be the same or different species. Temperature and velocities are assumed to be the same for both. Calculations of thermal conductivity, viscosity and average ionization state are also modified to account for multiple species.

Equation of state: $\quad P = P_{bulk} + P_{abl} = \left(\overline{\rho}_{bulk} + \overline{\rho}_{abl}\right)\tilde{R}\tilde{T}(1+\overline{z})$

Conservation of mass (source plasma): $\quad \dfrac{\partial\left(\overline{\rho}_{plasma}\tilde{v}_x\right)}{\partial x} + \dfrac{\partial\left(\overline{\rho}_{plasma}\tilde{v}_y\right)}{\partial y} = \quad 0$

Conservation of mass (ablated material): $\quad \dfrac{\partial\left(\overline{\rho}_{abl}\tilde{v}_x\right)}{\partial x} + \dfrac{\partial\left(\overline{\rho}_{abl}\tilde{v}_y\right)}{\partial y} = \dot{\beta}_{abl}\delta$

Mass fraction: $\quad f \equiv \dfrac{\overline{\rho}_{abl}}{\overline{\rho}}$, so $\overline{\rho}_{bulk} = \overline{\rho}(1+f)$ and $\overline{\rho}_{abl} = \overline{\rho}f$

The zero-gradient boundary conditions have been adopted for k and w at the freestream:

$$\frac{\partial k}{\partial y} = 0 \text{ and } \frac{\partial \omega}{\partial y} = 0$$

In fluid modeling, values of k and ω are typically specified at the free stream, based on experimental measurements [59,60]. Zero-gradient boundary conditions were adopted in this case because no such experimental data is available for the high temperatures and velocities of an ETC launcher. When benchmark cases were run, code results were the same with either of the above sets of boundary conditions.

Code Results for Test cases

Results of a benchmark case for turbulent flow are shown in Fig. 43. When surface ablation and radiation transport are neglected, the turbulent boundary layer can be described by looking at its behavior in several regions. Near the propellant surface ($y^+<5$) viscous stresses dominate, and the velocity profile follows the curve $u^+=y^+$. Away from the surface ($y^+>30$) turbulence dominates, and the profile follows the curve $u^+=5.61*\log(y^+)+4.9$, and between these two regions there is a transition region where the profile smoothly joins the two curves. Finally, at the outermost edge of the boundary layer the velocity profile is a function of the Reynolds number, and it rises above the logarithmic straight line. The case presented in Fig. 43 was a run at low temperature and velocity to test TURBFIRE results against those of the published EDDYBL code. The results of the two codes are nearly indistinguishable. The structure described above is evident in these results.
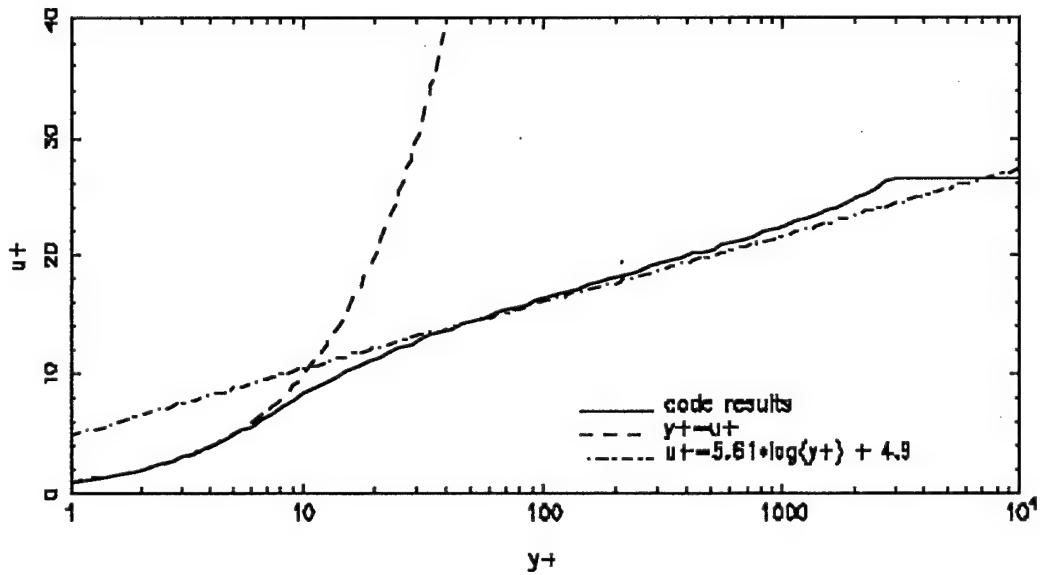
Fig. 43 Benchmark Case for Turbulent Flow. P=0.252bar, T_{wall}=242K, T_{fs}=217K, $v_{x,fs}$=295m/s

Figure 44 compares temperature profiles generated for higher velocity and temperature ($v_{x,fs}$=2km/s , T_{fs}=5eV) with and without turbulence, at a pressure of 1000 bar. The results show that turbulence increases the temperature near the surface and widens the boundary layer. This is expected to increase energy transfer to the propellant, and may thus enhance the burn rate. This

39

code run also illustrates the behavior of heat capacity and average ionization state in a plasma. Their profiles across the boundary layer are shown in Fig. 45. In previous versions of the code, ionization was not considered in the calculation of C_V. Accurate modeling of plasma heat capacity ($C_V = dU/dT$) has only recently been added to the model. The internal energy is the sum of the ionization and thermal energies, so the peaks in heat capacity correspond to regions where the ionization state increases rapidly with temperature. The importance of this change can be seen in Fig. 46, which shows the temperature profiles generated by running the code with a) constant heat capacity, b) heat capacity that varies smoothly with temperature (i.e. constant dC_V/dT), and c) $C_V = dU/dT$. The temperature profile for case c is higher through most of the boundary layer, so using either of the other models would underestimate heat flux to the propellant.
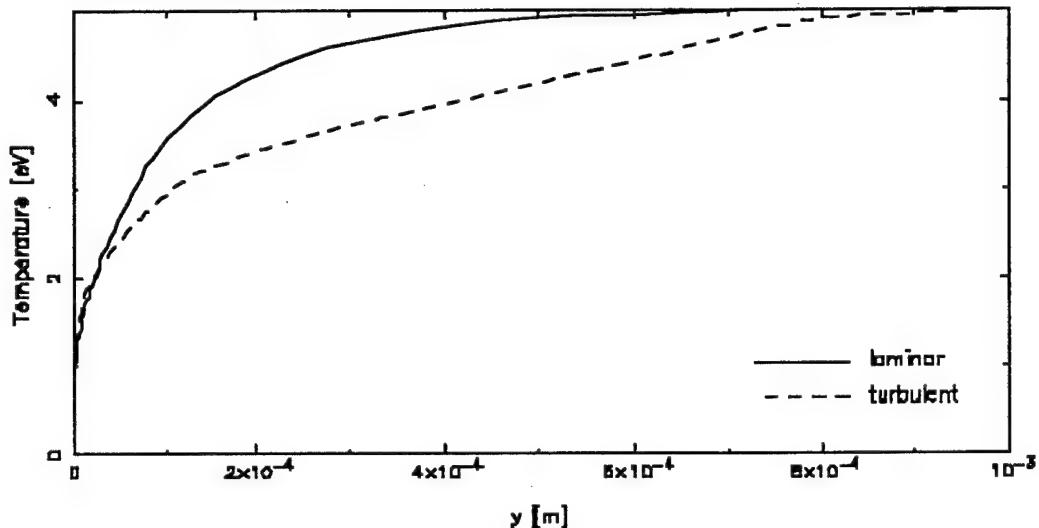
Fig. 44 Temperature Profiles for Laminar and Turbulent Flow. P=1000bar, T_{wall}=2000K, T_{fs}=5eV, $v_{x,fs}$=2km/s
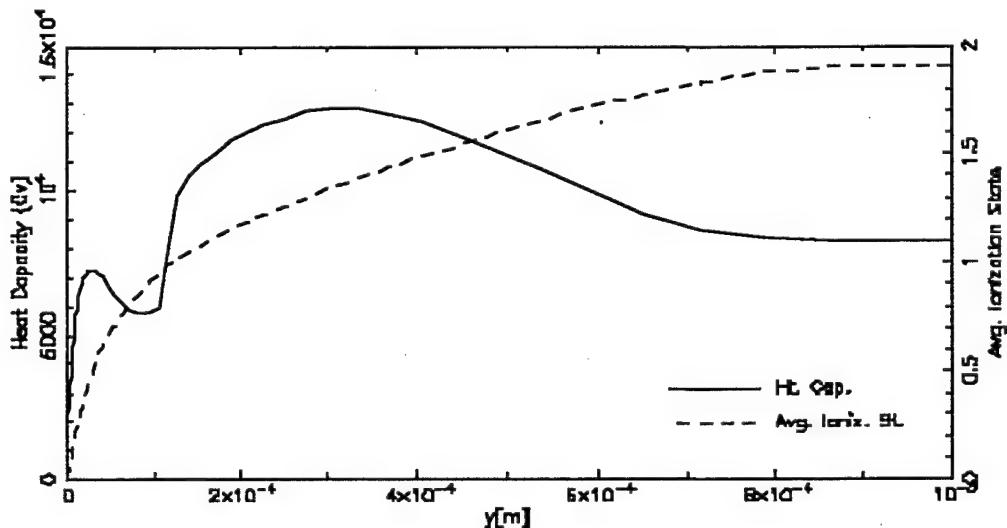

Fig. 45 Heat Capacity (C_V) and Average Ionization State ($\bar{z}$) for Turbulent Flow. P=1000bar, T_{wall}=2000K, T_{fs}=5eV, $v_{x,fs}$=2km/s

40
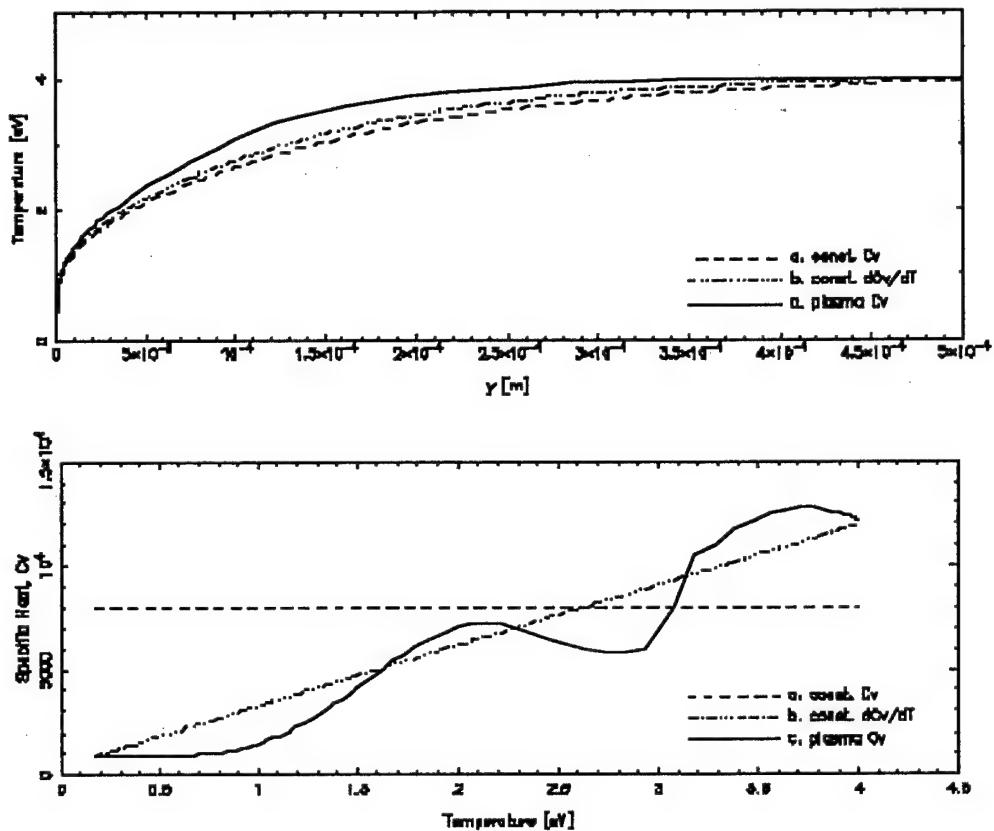
Fig. 46 A Comparison of Temperature Profiles Generated Using Three Models for C_V. P=1000bar, T_{wall}=2000K, T_{fs}=4eV, $v_{x,fs}$=1km/s

Preliminary results with both turbulence and radiation transport are shown in Fig. 47, which compares temperature profiles across the boundary layer with and without the turbulence and radiation transport models (T_{fs} = 2 eV, T_{wall}= 2000 K, u_{fs} = 1 km/s, and n_{wall} = 1.5×10^{22} cm^{-3}). These temperature profiles show that both turbulence and radiation heat the plasma near the propellant surface and cool the plasma farther away. Turbulence increases the temperature by as much as 6000K near the surface, and adding radiation increases the temperature by as much as 7000K above this. This higher near-wall temperature greatly increases heat flux to the surface, and is thus expected to effect the propellant burn rate. The results presented in Figure 5 were generated from code runs using with model b (above) for heat capacity. The code is currently being tested for radiation transport with the more accurate heat capacity model c. The effect of the heat capacity model is expected to be small everywhere except very close to the wall, since C_V appears only in the conduction term of the energy equation.
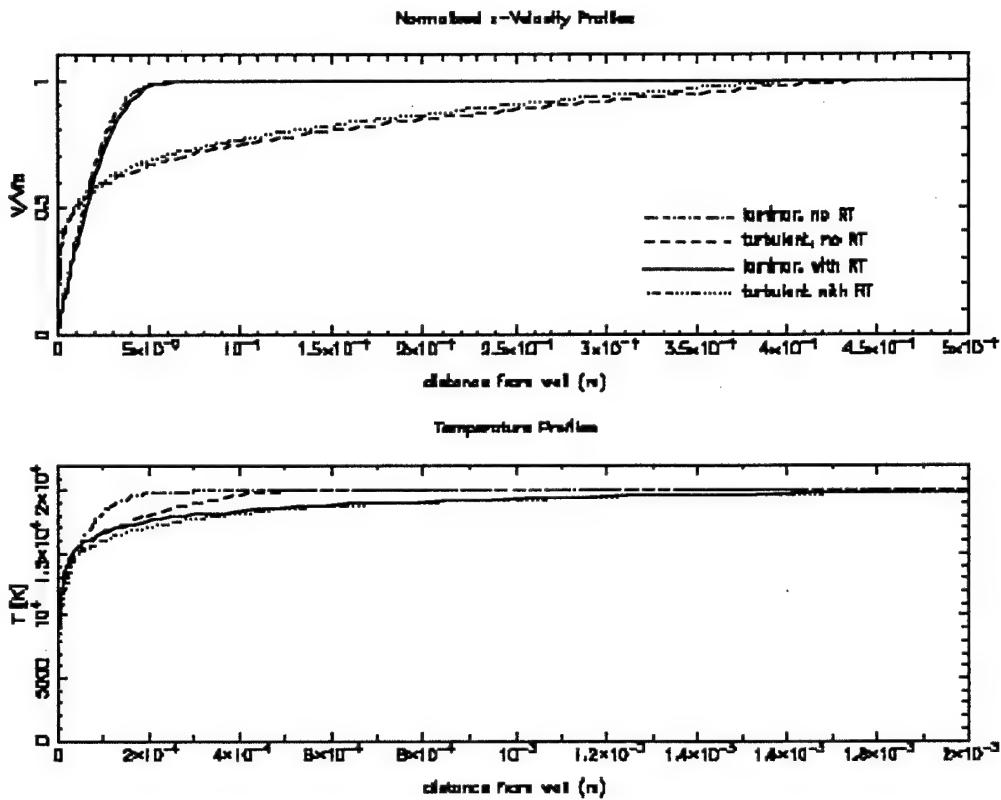
Fig. 47 Effects of Radiation and Turbulence on the Temperature Profile. T_{fs} = 20,000K, T_{wall} = 5,000K, u_{fs} = 1 km/s, and P = 1kbar

TURBFIRE results show that both radiation and turbulence are important factors in enhancing energy transport to the propellant in ETC devices. These results actually show more heating of the near-wall plasma that is seen experimentally. New models for heat capacity and thermal conductivity have been included in the code. Results of these changes show that conventional gas models for fluid properties are not adequate for modeling ETC plasmas. Zero-gradient boundary conditions have also been implemented for k and ω at the freestream. Results show that these changes do not change the results obtained when k_{fs} and ω_{fs} are specified, but the change was necessary since experimentally determined values of k_{fs} and ω_{fs} are not available for ETC conditions [61]. It will be important to know how radiation transport couples to combustion processes. Combustion may cause further shielding of the propellant from radiation, by creating a thermal shield at the flame temperature. However, interactions within combustible species and incoming plasma may play an additional role. The effect of magnetic fields on the damping of turbulence is also expected to be important, since this effect has been shown experimentally to be significant [62]. Damping of turbulence is expected to keep the inner vapor shield cooler with a subsequent drop in radiation transport to the propellant.

IX. CONCLUSIONS

Plasma-propellant interaction and effect of plasma parameters on gasification rate of JA-2 solid propellant have been experimentally investigated . The effect of individual plasma parameters on the gasification rate of JA2 has been studied by perturbing the plasma parameters at the source exit by attaching moderating sections to the source. Results showed an increase of JA-2 gasification rate with increased plasma temperature (radiation), while a pseudo pressure effect has been observed for single-side exposed samples. Gasification rate of JA-2 maintained its increase with plasma temperature for double-sided exposed samples with the disappearance of the negative pressure effect. The importance of the radiation effect reduces for previously exposed samples where permanent in-depth changes from the previous exposure do exist and affect the gasification rate. The effect of in-depth interaction between plasma radiation and JA-2 samples on the gasification rate has been studied by re-exposing the samples. A remarkable increase in the gasification rate has been observed with the double-sided exposed samples, which indicates that in-depth interaction between plasma radiation and propellant affects the gasification rate. Optical emission spectroscopy of the plasma jet at the source exit have shown C_2swan band as emission lines for low energy shots, and are noticed to undergo self-absorption in higher energy shots when moderating sections are attached to the source. Plasma temperatures obtained from optical emission spectroscopy are in good agreement with those predicted by the modified 1-D time dependent code, MODIN. Erosion and in-depth changes of the propellant grains have been observed by analyzing the samples using Scanning Electron Microscopy (SEM), where ablative features similar to that observed on solid materials exposed to radiation heat flux from electrothermal plasmas were observed.

The results of the developed pseudo 2-D, time dependent plasma generator code TITAN indicate that radial temperature gradients play a significant role in energy transfer and therefore cannot be neglected. However, variation of the current density within the plasma is minimal, though these small variations have a marked effect on the temperature distribution. Comparison of TITAN results with both experimentally obtained voltage traces, source exit pressure and spectroscopic analysis yield reasonable agreement. Time-averaged temperature from spectroscopic analysis was 2.27eV, while results from the TITAN code predict a time-averaged temperature of 2.42eV over the length of the source. Because the plasma expands at the source exit, the temperature at the exit will tend to be lower than at a point within the source, which explains the lower average temperature from spectroscopy than calculated by TITAN. The code predicted a peak pressure of 480MPa while the measured pressure was 500MPa. Code prediction of the plasma resistance was 0.1-0.15 Ω while measured resistance was 0.12 Ω. I addition, a comparison between TITAN results and MODIN (1-D, time-dependent plasma source code) predictions revealed good agreement between both codes and experimentally obtained data.

The results of the developed 2-D, time-independent code TURBFIRE show that both radiation and turbulence are important factors in enhancing energy transport to the propellant in ETC devices. These results actually show more heating of the near-wall plasma that is seen experimentally. It is expected that once the outlined ablation model is implemented, vapor shielding will reduce the surface heat flux to a realistic level. New models for heat capacity and thermal conductivity have been included in the code. Results of these changes show that conventional gas models for fluid properties are not adequate for modeling ETC plasmas. Zero-gradient boundary conditions have also been implemented for k and ω at the freestream. Results show that these changes do not change the results obtained when k_{fs} and ω_{fs} are specified, but the change is necessary due to the fact that experimentally determined values of k_{fs} and ω_{fs} are not available for ETC conditions.

X. REFERENCES

[1] W. Oberle and W. Morelli, "Current Activities in Electrothermal-Chemical Gun Propulsion in the United States", Proc. 28th JANNAF Combustion Subcommittee Meeting, CPIA Publication 573, vol.I, p. 75, Oct. 1991.

[2] R.L. Burton, B.K. Hilko and F.D. Witherspoon, "Heating of Liquid/Vapor Mixture by a Pulsed Electric Discharge", GT-Devices, Final Technical Report to Air Force Office of Scientific Research GTD 90-7, August 31, 1990.

[3] J.P. Warren, P. Parendo and M. Bradley, "Status of Electrothermal-Chemical Propulsion in 60mm Ammunition", Proc. 30th JANNAF Combustion Meeting, CPIA Publication 606, vol IV, pp.163-172, November 1993.

[4] J.D. Powell and J.H. Batteh, "Analysis of the Piccolo Injector for ETC Launch", Proc. 30th JANNAF Combustion Meeting, CPIA Publication 606, vol IV, pp.207-217, November 1993.

[5] L.E. Harris, et al., "Enhanced Propellant Burn Rate Through Plasma Erosion", Proc. 30th JANNAF Combustion Meeting, CPIA Publication 606, vol IV, pp.121-135, November 1993.

[6] M.A. Bourham, J. G. Gilligan, O.E. Hankins, W.Eddy, and J. Hurley. "Electrothermal Plasma Source as a High Heat Flux Simulator for Plasma-Facing Components and Launch Technology Studies", Proc. 9 International Conference on High Power Particle Beams, Washington, D.C., Vol. III, pp. 1979-1983,1992.

[7] M.A. Bourham, et al., "Investigation of Geometrical Influence on Plasma-Augmented Burn Rates of JA-2 Solid Propellant for ETC Guns" , Proc. 32nd JANNAF Combustion Meeting, NASA Marshall Space Flight Center, Huntsville, AL, CPIA Publications 631, Vol.1, pp.103-112, October 1995.

[8] C. Edwards, M. Bourham, and J. Gilligan. "Experimental Studies of the Plasma-Propellant Interface for Electrothermal Chemical Launchers", IEEE Trans. Magnetics, Vol. 31, pp. 404-409, Jan. 1995.

[9] L. Raja, P. Varghese and D. Wilson. "Modelling of Electrothermal Ignitor Metal Vapor Plasma for Electrothermal-Chemical Guns", IEEE Trans. Mag., Vol.33, No.l, pp. 316-321, January 1997.

[10] K. White, G. Katulka and S. Driesen, "Electro-Thermal Chemical Plasma Interaction with Propellants", Proc. 32nd JANNAF Combustion Meeting, CPIA Publication 631, Vol. 1, pp. 113-122, October 1995.

[11] M. Nusca and K. White, "Plasma Radiative and Convetive Interactions with Propellant Beds", Proc. 34th JANNAF Combustion Meeting, West Palm Beach, FL, CPIA Publications 662, Vol.I, pp. 21-33, 1997.

[12] D. H. Hahn and J. G. Gilligan, "Radiation Transport Through a Plasma Boundary Layer Between Armature and Material Surfaces", IEEE Trans. on Magnetics, Vol. 27, No. 1, p. 251, January, 1991.

[13] M.A. Bourham, O.E. Hankins, O.H. Auciello, J.M. Stock, B.W. Wehring, R.B. Mohanti and J.G. Gilligan, "Vapor Shielding and Erosion of Surfaces Exposed to High Heat Load in an Electrothermal Accelerator", IEEE Trans. on Plasma Science, Vol.17, pp. 386-391, June 1989.

[14] A.M. Hassanein, "Erosion and Redeposition of Divertor and Wall Materials During Abnormal Events", Fusion Technology, Vol.19, pp.1789-1793, May 1991.

[15] J.G. Gilligan and D.H. Hahn, "The Magnetic Vapor Shield (MVS) Mechanism for Protection of High-Heat Flux Components in High-Field Tokamaks", J. Nuclear Materials, Vol.145-147, pp. 391-395, 1987.

[16] M. A. Bourham, J. G. Gilligan, C. D. Buchanan and C. F. Boyer, "Effect of Electrothermal Plasma Parameters on the Burn Rates of JA-2 Solid Propellant for ETC Guns", Proc. 33rd JANNAF Combustion Meeting, CPIA Publication 653, Vol. 1, p. 57, November 1996.

[17] M. A. Bourham, J. G. Gilligan and W. F. Oberle, "Analysis of Solid Propellant Combustion Behavior Under Electrothermal Plasma Injection for ETC Launchers", IEEE Trans. on Magnetics, vol. 33, p. 278, January 1997.

[18] J.D Hurley, M. Bourham and J. Gilligan, "Modeling and Experiment of an Electrothermal Igniter for Electrothermal-Chemical Guns", Proc. 30th JANNAF Combustion Meeting, Monterey, CA, 15-19 November 1993, CPIA Publication 606, Vol.I, pp. 17-25, November 1993.

[19] J.D. Hurley, M.A. Bourham and J.G. Gilligan, "Numerical Simulation and Experiment of Plasma Flow in the Electrothermal Launcher SIRENS", IEEE Trans. Magnetics, Vol. 31, pp. 616-612, January 1995.

[20] D. Zoler and R. Alimi, "A Proof of the Need for Consistent Treatment in Modelling of Capillary Ablative Discharges", J. Phys. D: Applied Phys., Vol.28, pp. 1141-1152, 1995.

[21] R.W. Kincaid, Pellet Acceleration in an Electrothermal Plasma Gun, Ph.D. Thesis, North Carolina State University, 1995.

[22] R.W. Kincaid, M.A. Bourham and J.G. Gilligan, "Electrothermal Plasma Gun as a Pellet Injector", Fusion Technology, Vol.26, p.637, 1994.

[23] J. G. Gilligan and R. B. Mohanti, "Time-Dependent Numerical Simulation of Ablation-Controlled Arcs", IEEE Trans. Magnetics, Vol. 18, No. 21, p. 190, April 1990.

[24] E. Z. Ibrahim, "The Ablation Dominated Polymethylmethacrylate Arc", J. Phys. D.: Appl. Phys., Vol.13, p. 2045, 1980.

[25] C. B. Ruchti and L. Niemeyer, "Ablation Controlled Arcs", IEEE Trans. Plasma Sci., Vol. 14, p. 423, August 1986.

[26] J. D. Powell, A. E. Zielinski, "Theory and Experiment for an Ablating-Capillary Discharge and Application to Electrothermal-Chemical Guns", Tech. Report BRL-TR-3355, June 1992.

[27] A. Loeb and Z. Kaplan, "A theoretical Model for the Physical Processes in the Confined High Pressure Discharges of Electrothermal Launchers", IEEE Trans. on Magnetics, Vol. 25, pp. 342-346, January 1989.

[42] M.R. Zaghloul, S.K. Murali, J.G. Gilligan, O.E. Hankins and M.A. Boutham, "Analysis and Experimental Studies of Plasma-Propellant Interaction and Effect of Plasma Parameters on Burn Rates of JA2 Solid Propellant for ETC Guns", Proc. 35th JANNAF Combustion Meeting, Tucson, AZ, CPIA Publications 680, Vol. 1, pp. 247-257, December 1998.

[43] F.D. Witherspoon, R.L. Burton and S.A. Goldstein, "Railgun Experiments with Lexan Insulators", IEEE Trans. on Plasma Science, Vol. 17, pp.353-359, June 1989.

[44] J.O. Kolawole, R.V. Frierson, E.J. Clothiaux and C.E. Goodman, "Post-Shot Analysis of Plasma/Rail Interaction in a Small Bore Load Driving EML", IEEE Trans. on Magnetics, Vol.27, pp. 386-391, January 1991.

[45] M.A. Bourham, J.G. Gilligan, M.L. Huebschman, D. Lianos and P.D. Aalto, "Review of Components Erosion in Electric Launchers Technology", IEEE Trans. Magnetics, Vol. 31, pp.678-683, January 1995.

[46] Zollweg, R., and R. Liebermann. "Electrical Conductivity of Nonideal Plasmas", Journal of Applied Physics, Vol. 62, No. 9, pp. 3621-3627,1987

[47] R. B. Mohanti and J. G. Gilligan, "Electrical Conductivity and Thermodynamic Functions of Weakly Nonideal Plasmas", J. Appl. Phys. Vol. 68, pp.5044- 5051, November 1990.

[48] R. B. Mohanti, J. G. Gilligan, M. A. Bourham, "Time Dependent Simulation of Weakly Nonideal Plasmas in Electrothermal Launchers", Physics of Fluids B , Vol. 3, pp. 3046-3052, November 1991.

[49] L. Spitzer and R. Harm. "Transport Phenomena in a Completely Ionized Gas", Physical Review, Vol. 89, No. 5, pp. 977-981,1953.

[50] P. Kovitya, "Physical Properties of High-Pressure Plasmas of Hydrogen and Copper in the Temperature Range 5000-60000K", IEEE Trans. on Plasma Science, Vol. 13, No.6, pp. 587-594, Dec. 1 985 .

[51] M. Mitchner and C. Kruger, Partially Ionized Gases, Wiley & Sons, NY, 1973.

[52] Y. Zel'dovich and Y. Raizer. Physics of Shock Waves and High-Temperature Hydrodynamic Phenomena. Academic Press, NY, 1966.

[53] I. Shames, Mechanics of Fluids, 2nd ed., McGraw-Hill, NY, 1982.

[54] J. Powell, L. Thornhill and J. Batteh. "Current Distribution in Plasma Ignitors for ETC Launch", ARL Report, ARL-TR-1436, Sept., 1997.

[55] Powell, J. private communication.

[56] N. P. Orton and J. G. Gilligan, "Simulation of the Plasma-Surface Interaction in Electric Launchers", IEEE Trans. on Magnetics, vol. 31, p. 640, January 1995.

[57] G. Katulka, W. Oberle, G. Wren, J. Okamitsu and N. Messina, "Pulsed Power, Plasma and Interior Ballistic Simulation for Application to Electrothermal-Chemical Guns", Army Research Laboratory, ARL-TR-1070, March 1996.

[58] N. P. Orton, E. C. Tucker, J. G. Gilligan, J. M. Doster and M. A. Bourham, "Simulation of Plasma-Surface Interactions in Electro-Chemical Devices: Progress on the 2-D Code TURBFIRE", Proc. 34th JANNAF Combustion Meeting, CPIA Publication 662, Vol. 1, p. 57, October 1997.

[59] D. C. Wilcox, Turbulence Modeling for CFD, DCW Industries, 1994.

[60] F. R. Menter, "Influence of Freestream Values on k-ω Turbulence Model Predictions", AIAA Journal, Vol. 30, No. 6, p. 1657, 1992.

[61] N. P. Orton, J. M. Doster, J. G. Gilligan and M. A. Bourham, "TURBFIRE Simulation of Boundary-Layer Energy Transport and Vapor Shielding in Electrothermal-Chemical Launchers ", Proc. 35th JANNAF Combustion Meeting, Tucson, AZ, CPIA Publication 680, Vol. 1, pp. 211-218, December 1998.

[62] J. G. Gilligan, M. A. Bourham, O. E. Hankins and W. Eddy, "Magnetic Vapor Shielding Mechanism in Electromagnetic and Electrothermal Launchers", IEEE Trans. Magnetics, vol. 29, p. 1153, January 1993.

DISTRIBUTION

ADDRESSEES	NUMBER OF COPIES
Director (Acting) Dr. Spiro G. Lekoudis Mechanics & Energy Conversion Office of Naval rResearch 800 North Quincy Street Arlington, VA 22217-5660	2
Program Manager/Officer, ONR: 333 Dr. Judah M. Goldwasser Office of Naval rResearch Ballston Tower One 800 North Quincy Street Arlington, VA 22217-5660	3
Administrative Grants Officer Office of Naval Research Regional Office Atlanta 101 Marietta Street , Suite 2805 Atlanta, GA 30323-0008	1
Director, Naval Research Laboratory ATTN: Code 2627 Washington, DC 20375	1
Defense Technical Information Center 8725 John J. Kingman Road, STE 0944 Ft. Belvoir, VA 22060-6218	2

Engineering Research Administration College of Engineering North Carolina State University Box 7901 CAMPUS Raleigh, NC 27695-7901	2
Dr. Mohamed A. Bourham North Carolina State University Department of Nuclear Engineering Raleigh, NC 27695-7909	1
Dr. John G. Gilligan North Carolina State University Associate Dean, College of Engineering Raleigh, NC 27695-7901	1